AFRL-AFOSR-VA-TR-2019-0208

A Multi-Scale Approach of Combining Nano-indentation with Computational Mechanics to Predict Impact Behavior of Structural Composite Materials

Luoyu Xu
UNIVERSITY OF NEW MEXICO

10/22/2018
Final Report

Air Force Research Laboratory
AF Office Of Scientific Research (AFOSR)/ RTA1
Arlington, Virginia 22203
Air Force Materiel Command

DISTRIBUTION A: Distribution approved for public release.

REPORT DOCUMENTATION PAGE

Form Approved
OMB No. 0704-0188

1. REPORT DATE *(DD-MM-YYYY)*	2. REPORT TYPE	3. DATES COVERED *(From - To)*
24-07-2019	Final Performance	01 Nov 2017 to 31 Oct 2018

4. TITLE AND SUBTITLE
A Multi-Scale Approach of Combining Nano-indentation with Computational Mechanics to Predict Impact Behavior of Structural Composite Materials

5a. CONTRACT NUMBER

5b. GRANT NUMBER
FA9550-18-1-0006

5c. PROGRAM ELEMENT NUMBER
61102F

6. AUTHOR(S)
Luoyu Xu

5d. PROJECT NUMBER

5e. TASK NUMBER

5f. WORK UNIT NUMBER

7. PERFORMING ORGANIZATION NAME(S) AND ADDRESS(ES)
UNIVERSITY OF NEW MEXICO
1700 LOMAS BLVD NE
ALBUQUERQUE, NM 87106 US

8. PERFORMING ORGANIZATION REPORT NUMBER

9. SPONSORING/MONITORING AGENCY NAME(S) AND ADDRESS(ES)
AF Office of Scientific Research
875 N. Randolph St. Room 3112
Arlington, VA 22203

10. SPONSOR/MONITOR'S ACRONYM(S)
AFRL/AFOSR RTA1

11. SPONSOR/MONITOR'S REPORT NUMBER(S)
AFRL-AFOSR-VA-TR-2019-0208

12. DISTRIBUTION/AVAILABILITY STATEMENT
A DISTRIBUTION UNLIMITED: PB Public Release

13. SUPPLEMENTARY NOTES

14. ABSTRACT

This project is intended to break new ground in predicting the mechanical behavior of advanced composites across multiple time- (from slow nano-indentation to fast projectile impact) and length-scales (nanometers to inches). A combined experimental and computational approach is proposed, therefore, highly specializedand invariably time-consuming and expensiveimpact tests can be supplanted by simple nano-indentation tests and mechanics simulations. The outcome will allow efficient predictions of low-speed impact response and damage of composites. The project will also feature impact tests for validating the developed models and procedures. In this project, we conduct elastic nano-indentation experiments in order to obtain elastic properties for impact simulations, while impact damage and other nonlinear deformation beyond elastic deformation will be simulated by computational mechanics. Therefore, the major tasks of this project are listed below:
A. Conduct selected nano-indentation and other material characterization tests for composite systems to establish a mechanical property database at the material level.
B. Simulate the impact response and damage using the above material data.
C. Validate impact simulation using low-speed impact experiments of composite laminates.

15. SUBJECT TERMS
impact testing, carbon fiber composites, indentation tests

16. SECURITY CLASSIFICATION OF:				

a. REPORT	b. ABSTRACT	c. THIS PAGE	17. LIMITATION OF ABSTRACT	18. NUMBER OF PAGES	19a. NAME OF RESPONSIBLE PERSON
Unclassified	Unclassified	Unclassified	UU		TILEY, JAIMIE
					19b. TELEPHONE NUMBER *(Include area code)* 703-588-8316

Final Report to the US Air Force Office of Scientific Research

A Multi-Scale Approach of Combining Nano-indentation with Computational Mechanics to Predict Impact Behavior of Structural Composite Materials

AFOSR grant number FA9550-18-1-0006

Multiscale Structural Mechanics and Prognosis Program

Principal Investigator

Dr. L. Roy Xu, University of New Mexico

Project Period: November 2017—October 2018

October 20, 2018

1. Project Abstract

This project is intended to break new ground in predicting the mechanical behavior of advanced composites across multiple time- (from slow nano-indentation to fast projectile impact) and length-scales (nanometers to inches). A combined experimental and computational approach is proposed, therefore, highly specialized—and invariably time-consuming and expensive—impact tests can be supplanted by simple nano-indentation tests and mechanics simulations. The outcome will allow efficient predictions of low-speed impact response and damage of composites. The project will also feature impact tests for validating the developed models and procedures. In this project, we conduct elastic nano-indentation experiments in order to obtain elastic properties for impact simulations, while impact damage and other nonlinear deformation beyond elastic deformation will be simulated by computational mechanics. Therefore, the major tasks of this project are listed below:

A. Conduct selected nano-indentation and other material characterization tests for composite systems to establish a mechanical property database at the material level.

B. Simulate the impact response and damage using the above material data.

C. Validate impact simulation using low-speed impact experiments of composite laminates.

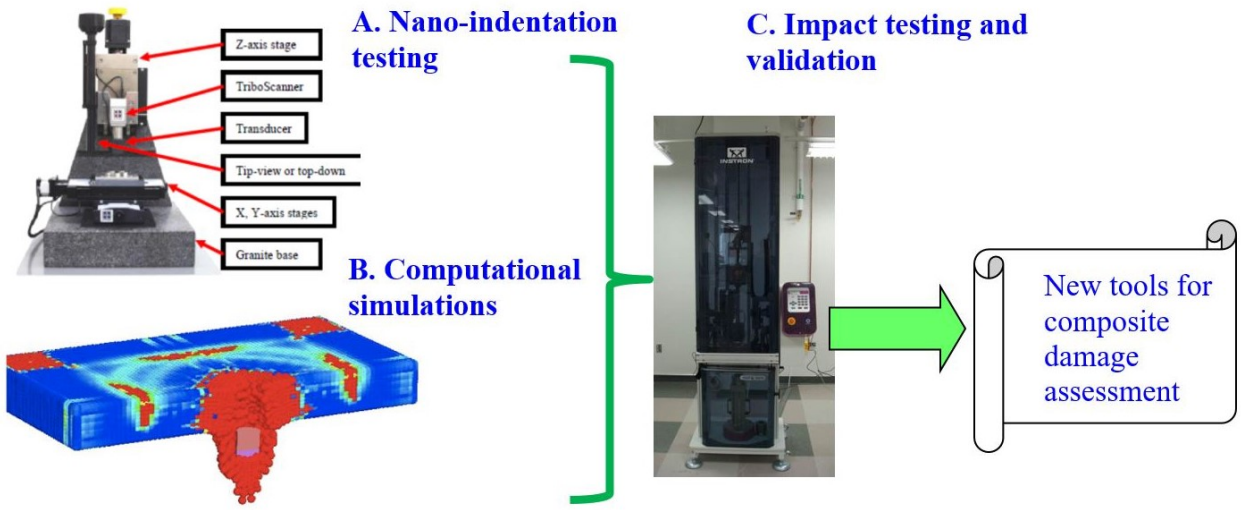

Figure 1. *Major research tasks of this project*

During the project period, we mainly have three major accomplishments:

1. We have developed a new approach to measure the through-thickness Young's moduli of composite materials using spherical nano-indentation and elastic loading curves. The measured Young's modulus of a glass fiber composite material was quite consistent with the reported modulus of a similar material system (difference 6.6%). The feature of our approach is its in-service Young's modulus measurements of composites as a function of service time.
2. We have developed a lower bound approach of the through-thickness Young's modulus measurement based on contact mechanics and micromechanics analysis. Therefore, the

proposed approach provides a conservative measurement if the actual through-thickness Young's modulus is not available. This approach is helpful for nanoindentation users without comprehensive knowledge of micromechanics and contact mechanics to deal with complicated composite indentation.

3. We have developed an efficient simulation approach combining multi-scale indentation mechanics and computational mechanics to predict the impact behaviors of composite laminates subject to low impact energy up to 10 J. The proposed statically equivalent simulation was validated by means of low-speed impact experiments of carbon/epoxy composite panels with four different stacking sequences. The proposed approach will provide simplified, yet conservative upper-bound estimates for damage and failure of composite laminates.

2. Brief Research Progress on Nanoindentation

2.1 Composite Young's moduli measured from the elastic loading curves and Hertz's law

The measurements of the through-thickness Young's moduli for composite laminates are very important because these parameters are related to impact response. We have developed a new approach to measure the through-thickness Young's moduli of composite materials using spherical nano-indentation and elastic loading curves. The measured Young's modulus of a glass fiber composite material (E-glass fiber/Vinyl Ester or EF/VE composite) was quite consistent with the reported modulus of a similar material system (difference 6.6%). The feature of our approach is its in-service Young's modulus measurements of composites as a function of service time.

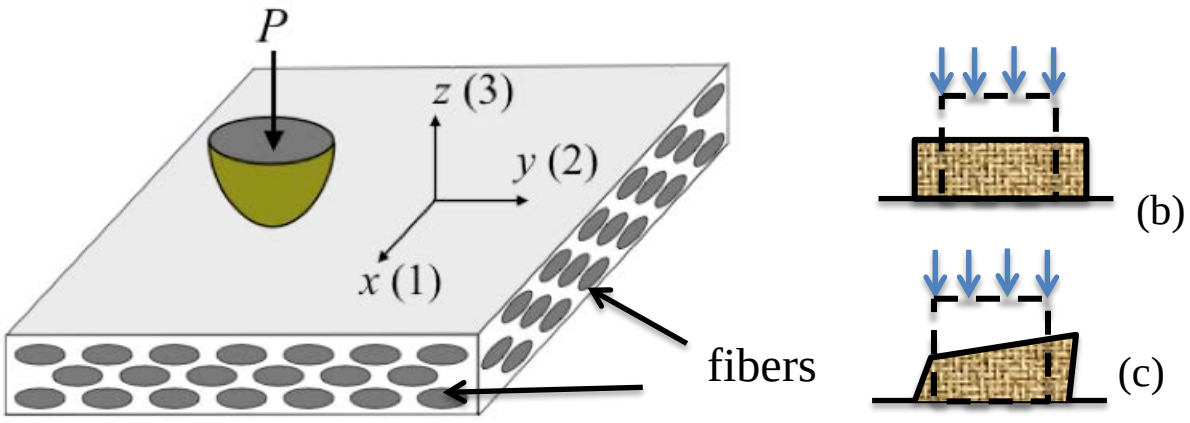

Figure 2. *Nanoindentation along the thickness direction (z or 3-direction) of a woven-fabric composite laminate (a), orthotropic laminates have normal strains under compressive load (b), anisotropic laminates have coupled normal and shear strains under the compressive load (c)*

The composite laminates must be orthotropic in order to avoid complicated deformation as shown in Figure 2. Because an indenter is perpendicular to the composite laminate, the measured Young's modulus is the through-thickness Young's modulus E_{33}. We proposed an approximate expression

of the reduced modulus E_r , which is related to E_{33}, Young's modulus E and the Poisson's ratio v of the indenter material (Martinez and Xu, 2018):

$$\frac{1}{E_r} \approx \frac{1-\nu_i^2}{E_i} + \frac{1-\nu_{31}\,\nu_{32}}{E_{33}} \approx \frac{1-\nu_i^2}{E_i} + \frac{1}{E_{33}} \qquad (1)$$

Here, a spherical indenter, rather sharp indenters should be employed to avoid any complicated phenomena (Johnson, 1985). In order to reduce the inhomogeneous effect of the composite modulus measurement, we recommend a spherical indenter with a large radius (>50 μm). A separation between two indents of 200 μm was sufficient. Moreover, we indent at least 100 locations on one composite specimen. The measured average through-thickness Young's modulus was 12.36 ± 4.13 GPa for the EF/VE composite system, while the theoretical lower bound of the modulus is 6.85 GPa. The above results demonstrated that the nanoindentation test can replace the complicated through-thickness waisted block test for the through-thickness modulus measurement (Daniel and Ishai, 2005). One journal paper is under review (Appendix).

2.2 Micromechanics characterization on the lower bound Young's moduli measurement

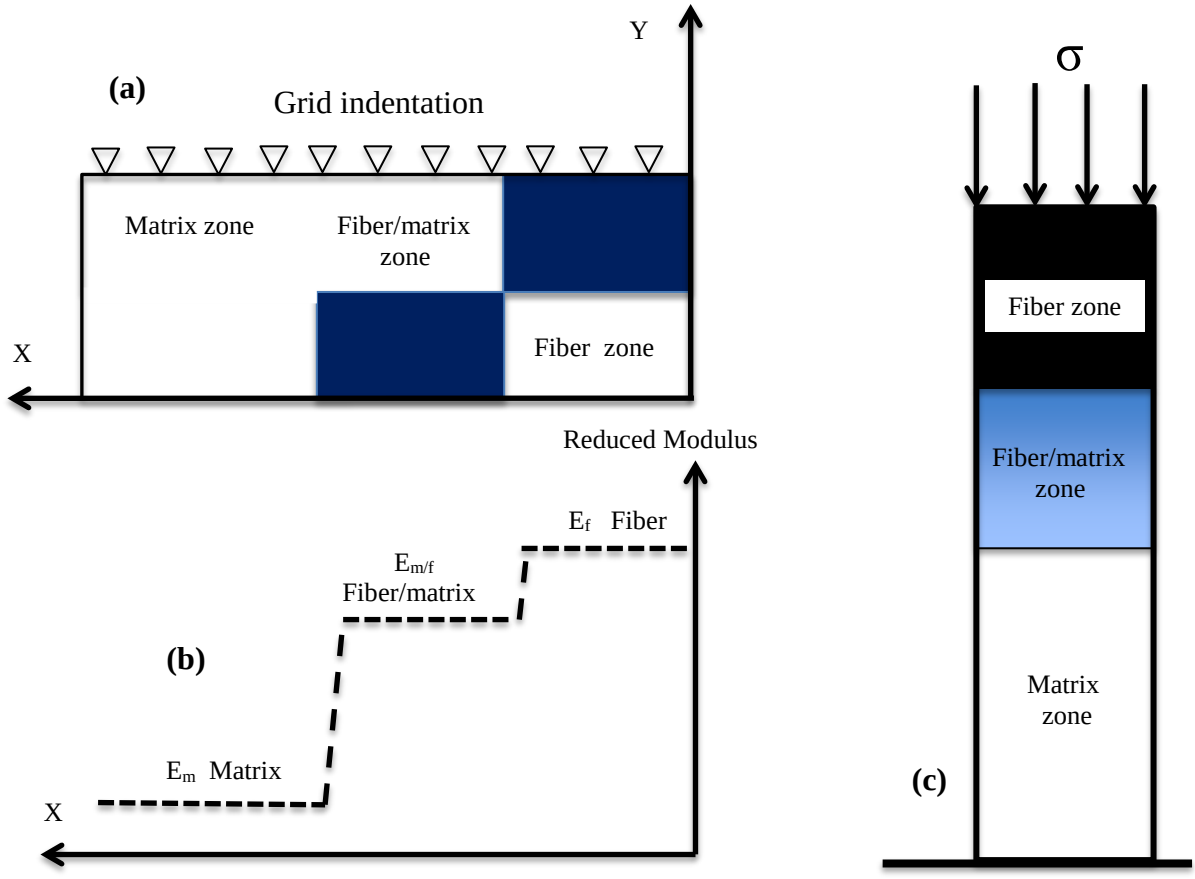

Figure 3. *Illustrations of (a) grid nanoindentation on a composite surface, (b) measured reduced modulus distributions, (c) a series model including the fiber, the matrix and mixed zones.*

If we use a sharp indenter to conduct grid nanoindentation on a composite surface, we cannot measure the through-thickness Young's modulus. However, we can obtain a lower bound of the moduli using nano-indentation unloading curves (Oliver and Pharr, 1992) based on contact mechanics and micromechanics analysis. This approach was applied to a glass-fiber composite material system, and the estimated lower bound was around 40% lower than the measured Young's modulus of the same composite system using Hertz's contact law and elastic loading curves. Therefore, the proposed approach provides a conservative measurement if the actual through-thickness Young's modulus is not available. This approach is also helpful for nanoindentation users without comprehensive knowledge of micromechanics and contact mechanics to deal with complicated composite indentation. One journal paper is under review for this topic (Appendix).

The lower bound of the through-thickness Young's modulus based on composite nanoindentation can be expressed as follows (Xu et al, 2018):

$$E_{33} > 0.75 \Big/ \left[\frac{N_f}{N_T\, E_r^f} + \frac{N_m}{N_T E_r^m} + \frac{N_{m/f}}{N_T E_r^{m/f}} \right] \approx 0.75 N_T \left[\sum_{j=1}^{N_T} \frac{1}{E_r^j} \right]^{-1} \quad (2)$$

where E_r^f , E_r^m and $E_r^{f/m}$ are the reduced moduli of the fiber, the matrix and the mixed fiber/matrix zones. N_T is the total grid indentation number, and N_f, N_m, $N_{f/m}$ and the numbers of grid indentations on the fiber, matrix and mixed zones. We find that the measured lower bound Young's modulus of the EG/VE composite system is 7.68 GPa. While the average through-thickness composite Young's modulus measured from a spherical indentation was 12.36 GPa (Martinez and Xu, 2018), and it ranged from 8.23 to 16.49 GPa. Therefore, 7.68 GPa is indeed a lower bound since it is smaller than the directly measured Young's moduli. Moreover, this lower bound modulus could be predicted by the series rule-of-mixture model, and the theoretical lower bound of the composite modulus is 6.85 GPa, which is quite close to the experimental lower bound 7.68 GPa. For structural materials, a low material property is very important due to the safety concern, e.g., a low fracture toughness should be measured only under the plane-strain condition. Therefore, our lower bound approach will enhance the safety of composite structures.

2.3 Influence of the stacking sequences on the composite through-thickness Young's moduli measured by nanoindentation.

Nanoindentation specimens of carbon fiber/epoxy IM7/977-3 composites were provided by the Air Force Research Laboratories (AFRL). These specimens have four different stacking sequences with 24 plies (Flores et al, 2017**).** Stacking sequences are panel A $[-45/90/45/90/-45/0/45/90/90/-45/90/45]_s$, panel B $[-45/45/-45/45/0/45/90/-45/45/-45/45/-45]_s$, panel C $[-45_3/90_3/45_3/0_3]_s$, and panel D $[-45/90/45/0]_{3s}$. All specimens have the same size 25.4 mm x 25.4 mm. A spherical indenter with a large radius (200 μm) was used to conduct nanoindentation tests on an I-Micro Nano Indenter. Total indentations were 25 for each specimen, and the minimum indentation depth was 300 nm to ensure full deformation of a representative volume element (RVE) and eliminate the surface roughness effect. Selected loading and unloading indentation curves were very close and no permanent deformation was found. Based on the data reduction process described in 2.1, the measured through-thickness Young's moduli are listed in Table 1.

The Young's moduli of four stacking sequences are close (maximum difference < 23%). Usually, the in-plane stiffness properties of a composite laminate can be determined by lamination theory. However, the strain along the laminate thickness direction is assumed to be zero in lamination theory (Daniel and Ishai, 2005), so the through-thickness stiffness properties cannot be determined by lamination theory. Or there is no direct relation between the stacking sequence and the through-thickness Young's modulus. If we use the rule-of-mixture to evaluate the through-thickness Young's moduli, since the fiber volume percents and the fiber/matrix are the same for these four laminates, their Young's moduli should be close.

Table 1. Comparison of the through-thickness Young's moduli of four composite laminates

Composite panel	Young's modulus (GPa)	Difference (%)
A	7.9	baseline
B	8.4	+6.3
C	9.1	+15.2
D	9.7	+22.7

3. Brief Research Progress on Impact Experiments

Impact specimens of carbon fiber reinforced epoxy IM7/977-3 were provided by AFRL and panels A, B, C and D had four stacking sequences. All specimens have the same sizes of 101.6mm (width), 152.4 mm (length) and 3.2 mm (thickness) according to ASTM standard 7136 for composite impact experiments. Before impact experiments, all specimens were C-scanned to determine if any initial damage defects.

During impact tests, composite specimens were clamped onto a fixture with a rectangular open frame. This impact fixture was fixed to a steel base inside a drop weight tower. The impact event was introduced using a DYNATUP drop weight tower with a 15.9 mm (5/8 inch) diameter hemispherical tupper (mass of 3.37 kg). Each impact (impact energy 5 J) occurred in the center of the specimen, which was enough energy to create internal damage. The average peak loads for panel A, B, C, and D are 3.76 kN, 3.96 kN, 3.27 kN, and 3.89 kN, respectively. Only panel C showed one matrix crack on the bottom surface, while no external damage was found from other panels. Our impact experiments were highly repeatable.

4. Brief Research Progress on Numerical Simulation

4.1. Composite damage modelling

The composite damage model is a combination of intra- and inter-laminar damage models. The intra-laminar damage was modeled through three-dimensional Hashin (1980) damage model adopted from ABAQUS for which compressive/tensile matrix and fiber failure modes were separately treated. The inter-laminar damage modeling is based on cohesive behavior between the plies of a composite laminate. The damage initiation is governed by quadratic-traction-separation law (Zhang and Zhang, 2015):

$$\left(\frac{t_n}{N}\right)^2+\left(\frac{t_s}{S}\right)^2+\left(\frac{t_t}{T}\right)^2\geq 1, \tag{3}$$

in which t_n, t_s, t_t are the interface stresses in the normal and two shear directions, respectively and N, S, T are corresponding strengths. In this expression, no irreversible deformation occurs till the tractions, or interfacial stresses, reach a peak value (or initiation of damage). Thereafter, cohesion between the plies will decrease with decreasing traction and increasing separation. During this phase, damage evolution occurs, which describes the degradation of cohesive stiffness between the plies. Here, fracture energy based mixed-mode damage evolution law is used to describe the dependency of the fracture modes so that

$$\left(\frac{G_I}{G_{IC}}\right)+\left(\frac{G_{II}}{G_{IIC}}\right)+\left(\frac{G_{III}}{G_{IIIC}}\right)\geq 1. \tag{4}$$

Here, G_I, G_{II}, G_{III} are the strain energy release rates under the modes I, II, and III, respectively while $G_{IC}, G_{IIC}, G_{IIIC}$ are the interlaminar fracture toughnesses for different fracture modes. Since we simulated the low-speed impact problem (impact energy < 10 J), the strain rate effect of the above material constants was not included. Material properties of IM7/977-3 composites were reported by AFRL researchers (Clay and Knoth, 2017; Hoos et al., 2017).

4.2. Comparison with experimental results and discussion

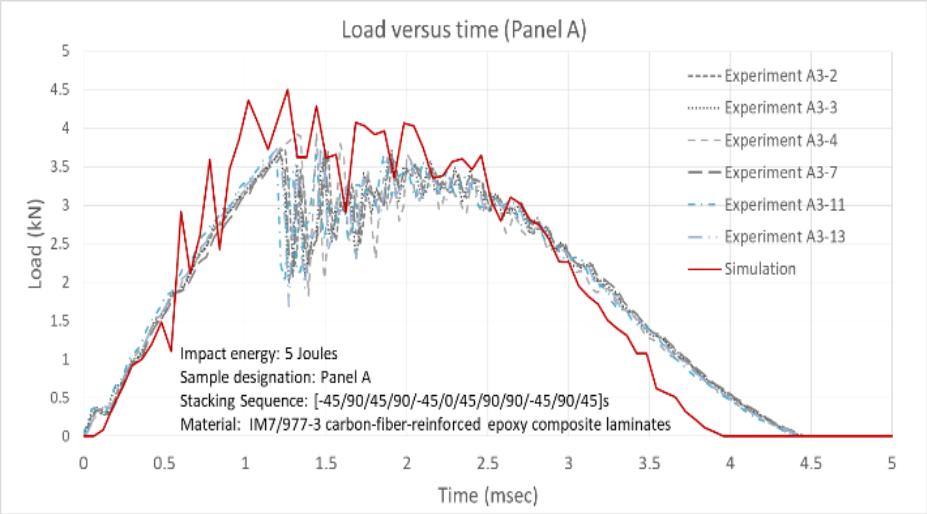

***Figure 4**: Impact load history comparison of panel A—simulations and experiments.*

Panels with four different stacking sequences A-D were investigated under the impact energy of 5 and 10 J. Two types of simulations, which are regular dynamic and our proposed efficient equivalent force simulations (§ 2 of our original proposal), were designed and conducted in the

scheme of explicit time integration. The dynamic simulations were used to check the prediction accuracy of the proposed model by comparing the simulation and experimental load history under the impact energy of 5 J. The efficient simulations were employed to determine the maximum damage area as a function of the maximum impact load P_{max} derived from our multi-scale indentation method. The damaged areas from simulations were compared with our new experimental results (impact energy of 5 J) and the AFRL's previous results (impact energy of 10 J) reported by Flores et al. (2017). As a result of these simulations, impact load history of four panels were compared with the experimental data as seen in Figure 4. Here we only show the results of panel A because results for other panels were quite consistent. It is noticed that our six experimental curves are highly repeatable, or six curves look like one curve. The simulated load history generally agrees with the experimental history. However, the simulated impact force was somewhat higher than the measured value. We believe that this discrepancy was caused by inaccurate material constants such as the interlaminar shear strengths S,T (we had to use assumed values from other papers), so we will measure these key constants in our future work. Figure 5 shows the simulated damage areas of two panels under impact energy of 5 J. Our AFRL collaborator just completed C-scanning of the impacted specimens and found the maximum impact damage size (one direction) was around one inch or 12 mm. Our simulated maximum damage size is around 10-16 mm.

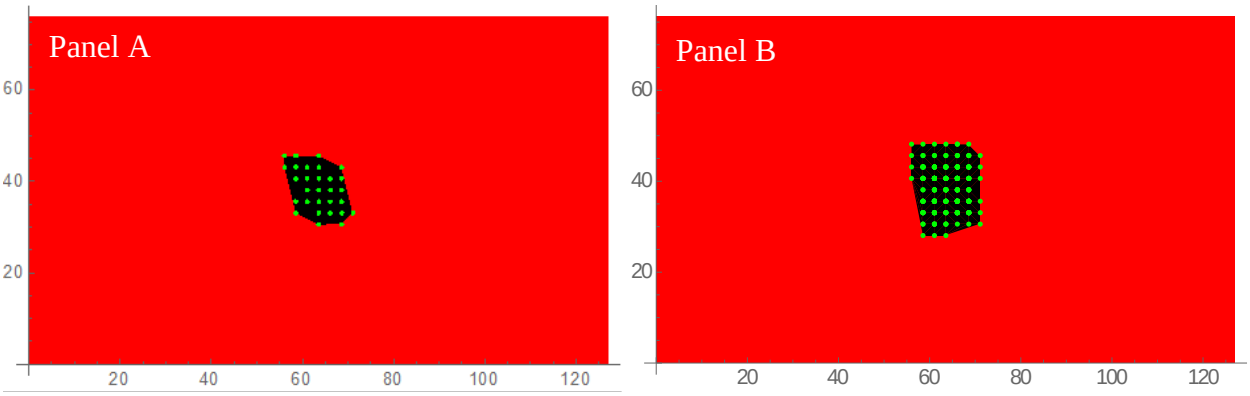

Figure 5. *Simulated impact damage areas of two panels under 5 J impact energy.*

One efficient simulation was conducted to obtain the impact damage in four panels subjected to 10 J impact, and the results are shown in Table 2. We notice that for panels A, B and D, the simulated damage areas are 20-30% larger than the measured areas. This was the feature we expected, because 1) we only focused on indentation deformation and energy in our efficient simulations, while bending deformation was not included, and 2) a large simulated damage area is helpful for conservative damage tolerance design especially in the early composite design stage. For panel C, a large discrepancy between the simulated and measured damage areas existed. This is not a surprising result because the AFRL team has noticed that panel C has small bending stiffness or large bending deformation (Flores et al., 2017). So, its impact peak load and maximum damage area were very different from other panels. Almost all aerospace composite structures have large bending stiffnesses or small deformation, so our efficient simulation is applicable. One journal paper is under review for this topic (Appendix).

Table 2. Comparison of measured and simulated impact damage areas (impact energy 10 J)

Composite panel	Measured area (mm^2)	Simulation (mm^2)	Notes
A	704.9	824.0	
B	571.4	761.6	
C	2545.4	1432.7	Small bending stiffness
D	704.9	874.4	

References

Bogdanor M, Oskay C, Clay SB (2015). Multiscale modeling of failure in composites under model parameter uncertainty. Computational Mechanics, 56:389–404.

Clay SB, Knoth PM, (2017). Experimental results of quasi-static testing for calibration and validation of composite progressive damage analysis methods, Journal of Composite Materials, 51, 1333-1353.

Duan C, Hodge AM (2009). High-temperature nanoindentation: new developments and ongoing challenges. Journal of the Minerals, Metals & Materials Society, 61: 32-36.

Daniel IM, Ishai O (2005). Engineering Mechanics of Composite Materials. Oxford University Press, New York.

Daniel IM, Luo J-J, Schubel PM, Werner BT (2009). Inter-fiber/interlaminar failure of composites under multi-axial states of stress. Composites Science and Technology, 69: 764–771.

Flores M, Mollenhauer DH, Runatunga V, Beberniss T, Rapking D, Pankow M, (2017). High-speed 3D digital image correlation of low-velocity impacts on co mposite plates, Composites Part B, , 131, 153-164.

Flores M. 2017-2018, private communication.

Hashin Z (1980). Failure criteria for unidirectional fiber composites. Journal of Applied Mechanics, 47, 329-334.

Hoos K, Iarve EV, Braginsky M, Zhou E, Mollenhauer DH, (2017). Static strength prediction in laminated composites by using discrete damage modeling, Journal of Composite Materials, 51, 1473-1492.

Jung J, **Taciroglu** E (2016). "A divide-alternate-conquer approach to localization and shape identification of multiple scatterers in elastic heterogeneous media using dynamic XFEM," Inverse Problems and Imaging, 10(1), 165-193.

Jung J, **Taciroglu** E (2014). "Modeling and identification of an arbitrarily shaped scatterer using dynamic XFEM with cubic splines," Computer Methods in Applied Mechanics and Engineering, 278: 101-118.

Johnson K L Contact Mechanics (1985). Cambridge University Press, Cambridge, England.

Karbhari VM, Rydin RW (1999). Impact characterization of RTM composites—II: damage mechanisms and damage evolution in plain weaves. J. Mater. Sci., 34, 5641–5648.

Krishnan A, **Xu LR** (2011). A short-beam shear fracture approach to measure the mode II fracture toughness of materials with preferred interfaces. International J Fracture, 169: 15-25.

Ling D, Yang Q, Cox B (2009). An augmented finite element method for modeling arbitrary discontinuities in composite materials. Int. J. Fracture, 156: 53-73.

Martinez R, **L R Xu** (2018). Approximate Measurements of the Though-Thickness Young's Moduli of Fibrous Composite Laminates using Nanoindentation, submitted for publication.

Oliver W C and Pharr G M (1992). An improved technique for determining hardness and elastic modulus using load and displacement sensing indentation experiments, Journal of Materials Research 7 1564-1583

Sun CT, Han C (2004). A method for testing interlaminar dynamic fracture toughness of polymeric composites. Composites Part B: 35: 647-655.

Tsai SW, Wu EM (1971). A general theory of strength for composite materials, Journal of Composite Materials, 5(1): 58-80.

Wang P, **Xu LR** (2006) Dynamic Interfacial Debonding Initiation Induced by An Incident Crack," International Journal of Solids and Structures, 43, 6535-6550.

Xu LR, Rosakis AJ (2002). Impact failure characteristics in sandwich structures:: P art I: Basic failure mode selection." International journal of solids and structures, 39: 4215-4235.

Yaghoub AS, Liaw B (2012). Thickness influence on ballistic impact behaviors of GLARE 5 fiber-metal laminated beams: Experimental and numerical studies. Comp. Struct., 94: 2585-2598.

Yan H, Oskay C, Krishnan A, **Xu LR** (2010). Compression After Impact Response of Woven Fiber-Reinforced Composites. Composites Science and Technology, 70: 2128-2136.

Xu L R Martinez R., Zhao, K. (2018). Micromechanics Characterization on the Lower Bound Young's Moduli of Composite and Heterogeneous Materials Measured from Nanoindentation, submitted for publication.

Zhang J, Zhang X, (2015). An efficient approach for predicting low-velocity impact force and damage in composite laminates, Composite Structures, 130, 85-94.

Appendix

Three journal papers under review

Integrated Numerical and Experimental Studies on Dynamic Responses of Composite Laminates Subjected to Low-energy Impact

Alp Karakoç[1,*], L. Roy Xu[2], Ertugrul Taciroglu[1], Mark Flores[3], Haibin Ning[4]

[1]Civil and Environmental Engineering, University of California Los Angeles, CA 90095, USA

[2]Department of Mechanical Engineering, University of New Mexico, Albuquerque, NM 87131, USA

[3] Air Force Research Laboratory, Wright-Patterson AFB, OH 45433, USA

[4] Department of Materials Science and Engineering, University of Alabama, Birmingham, AL 35294, USA

ABSTRACT

Despite the favorable directional and specific properties of composite laminate, their resistance against out-of-plane impact is a major concern. Although numerous papers reported simulations or experimental studies on impact damage of composite laminates, very few papers addressed integrated simulation and experimental studies. Therefore, the present study introduces a new simulation approach combining indentation mechanics and computational mechanics to predict the impact behaviors of composite laminates subject to low impact energy (5 and 10 J). The proposed statically equivalent simulation was validated by means of low-speed impact experiments and numerical simulations of carbon/epoxy IM7/977-3 composite panels with four different stacking sequences. The simulated impact load history, maximum damage areas, average peak loads and displacements of composite panels with large bending stiffness (panel A, B and D) were in generally good agreement with the measurements. Due to the exclusion of bending deformation, the simulated maximum damage areas of panel A, B and D are always larger than the measured areas. However, relatively large simulated damage areas are helpful for conservative damage tolerance design. The exclusion of bending deformation is reasonable because almost all aerospace composite structures have large bending stiffnesses or small bending deformation. Eventually, the proposed approach will provide simplified, yet conservative upper-bound estimates for damage and failure of composite laminates.

Keywords: composite laminate, low-speed impact, indentation mechanics, damage.

* Corresponding author's e-mail address: akarakoc@alumni.ucla.edu (Alp Karakoç).

1. INTRODUCTION

Composites have been increasingly used as structural components in aerospace industries, and other industries. Despite their favorable directional and specific properties, their resistance against out-of-plane impact is a major concern (Singh et al., 2017). Especially, low-speed impact, e.g., tool drops during a routine maintenance, bird strike or hail impact, can cause invisible or barely visible damage and may readily lead to in-service failure (Abrate, 1991; Choi et al., 1991; Rhymer et al., 2012; Xu et al., 2012; Sepe et al., 2016). Therefore, it is important to develop numerical tools for predicting the behavior and assessing the intra- and interlaminar damage of structural composites subjected to low-speed impacts. For this purpose, the current study represents a numerical approach combining the indentation mechanics principles and computational mechanics, which has been applied to composite laminates of four different stacking sequences. Although numerous papers reported simulations or experimental studies on impact damage of composite laminates (Sun and Rechak,1988; Lambros and Rosakis, 1997; Geubelle and Baylor, 1998; Karbhari and Rydin, 1999; Xu and Rosakis, 2002), very few papers addressed integrated simulation and experimental studies (Yan et al., 2010; Yaghoub and Liaw, 2012; Zhang and Zhang, 2015).

In the present study, the intra-laminar damage is modeled with four distinct failure mechanisms, namely compressive /tensile matrix and fiber failure modes. On the other hand, the interlaminar damage is modeled as surface-based cohesion between each lamina, for which the cohesive behavior is characterized with damage initiation and damage evolution laws. As a novelty, the impact loading condition for the statically equivalent simulations is formulated with the indentation principles, which aims at simplifying the complicated computations and reducing the computational cost. The present approach is thus believed to provide a foundation for the composite damage investigation, especially in the field of low-speed impact.

2. METHODOLOGY

2.1. Composite damage modelling

The present composite damage model is a combination of intra- and interlaminar damage models. The intra-laminar damage was modelled through 3-D Hashin damage model coded as VUMAT user subroutine for Abaqus/Explicit based on (ABAQUS, 2009; Nie, 2014), for which the compressive / tensile matrix and fiber failure modes were separately treated. In the intra-laminar damage model, the calculations start with computing initial or undamaged orthotropic elastic parameters C_{ij}^{0} (i,j=1,2,3) as

$$
\begin{aligned}
C_{11}^0 &= E_{11}(1-\nu_{23}\nu_{32})\Gamma,\\
C_{22}^0 &= E_{22}(1-\nu_{13}\nu_{31})\Gamma,\\
C_{33}^0 &= E_{33}(1-\nu_{12}\nu_{21})\Gamma,\\
C_{12}^0 &= E_{11}(\nu_{21}+\nu_{31}\nu_{23})\Gamma,\\
C_{23}^0 &= E_{22}(\nu_{32}+\nu_{12}\nu_{31})\Gamma,\\
C_{13}^0 &= E_{11}(\nu_{31}+\nu_{21}\nu_{32})\Gamma,\\
\Gamma &= 1/(1-\nu_{12}\nu_{21}-\nu_{23}\nu_{32}-\nu_{31}\nu_{13}-2\nu_{21}\nu_{32}\nu_{13}).
\end{aligned}
\tag{1}
$$

The damaged parameters C_{ij} are then determined as

$$
\begin{aligned}
C_{11} &= (1-d_f)C_{11}^0,\\
C_{22} &= (1-d_f)(1-d_m)C_{22}^0,\\
C_{33} &= (1-d_f)(1-d_m)C_{33}^0,\\
C_{12} &= (1-d_f)(1-d_m)C_{12}^0,\\
C_{23} &= (1-d_f)(1-d_m)C_{23}^0,\\
C_{13} &= (1-d_f)(1-d_m)C_{13}^0,\\
G_{12} &= (1-d_f)(1-d_{mt})(1-d_{mc})G_{12}^0,\\
G_{23} &= (1-d_f)(1-d_{mt})(1-d_{mc})G_{23}^0,\\
G_{31} &= (1-d_f)(1-d_{mt})(1-d_{mc})G_{31}^0,
\end{aligned}
\tag{2}
$$

for which the global fiber failure d_f and matrix failure d_m variables are

$$
\begin{aligned}
d_f &= 1-(1-d_{ft})(1-d_{fc}),\\
d_m &= 1-(1-d_{mt})(1-d_{mc}).
\end{aligned}
\tag{3}
$$

In Equations (2) and (3), d_{ft}, d_{fc}, d_{mt} and d_{mc} are the local damage variables for the tensile/compressive fiber and tensile/compressive matrix failure modes, respectively. For the known stress σ_{ij} and the tensile/compressive longitudinal strength X_{1T}, X_{1C}, the tensile/compressive transverse strength X_{2T}, X_{2C} and shear strength parameters X_{1S}, X_{2S}, these local damage variables are expressed as

$$
d_{ft} = \left(\frac{\sigma_{11}}{X_{1T}}\right)^2 + \left(\frac{\sigma_{12}}{X_{1S}}\right)^2 + \left(\frac{\sigma_{13}}{X_{2S}}\right)^2, \tag{4}
$$

$$
d_{fc} = \left(\frac{\sigma_{11}}{X_{1C}}\right)^2, \tag{5}
$$

$$d_{mt,mc} = \left[\left(\frac{\sigma_{11}}{2X_{1T}} \right)^2 + \left(\frac{\sigma_{22}}{\left| X_{2T} X_{2C} \right|} \right)^2 + \left(\frac{\sigma_{12}}{X_{1S}} \right)^2 \right] + \sigma_{22} \left[\frac{1}{X_{2T}} + \frac{1}{X_{2C}} \right] = \begin{cases} d_{mt}, & \text{when } \sigma_{22} + \sigma_{33} > 0 \\ d_{mc}, & \text{when } \sigma_{22} + \sigma_{33} < 0 \end{cases}. \tag{6}$$

The damaged elastic stress-strain matrix is eventually represented as

$$\begin{Bmatrix} \sigma_{11} \\ \sigma_{22} \\ \sigma_{33} \\ \sigma_{12} \\ \sigma_{23} \\ \sigma_{31} \end{Bmatrix} = \begin{pmatrix} C_{11} & C_{12} & C_{13} & 0 & 0 & 0 \\ C_{12} & C_{22} & C_{23} & 0 & 0 & 0 \\ C_{13} & C_{23} & C_{33} & 0 & 0 & 0 \\ 0 & 0 & 0 & 2G_{12} & 0 & 0 \\ 0 & 0 & 0 & 0 & 2G_{23} & 0 \\ 0 & 0 & 0 & 0 & 0 & 2G_{31} \end{pmatrix} \begin{Bmatrix} \varepsilon_{11} \\ \varepsilon_{22} \\ \varepsilon_{33} \\ \varepsilon_{12} \\ \varepsilon_{23} \\ \varepsilon_{31} \end{Bmatrix}. \tag{7}$$

The interlaminar damage modeling is based on the cohesive behavior between the plies of the composite laminate. The damage initiation is governed by the quadratic-traction-separation law

$$\left(\frac{t_n}{N} \right)^2 + \left(\frac{t_s}{S} \right)^2 + \left(\frac{t_t}{T} \right)^2 \geq 1, \tag{8}$$

in which t_n, t_s, t_t are the interface stresses in the normal and two shear directions, respectively and N, S, T are the interfacial normal and shear strengths. In this expression, no irreversible deformation occurs till the tractions, or the interfacial stresses, reach a peak value, i.e. initiation of the damage. Thereafter, the cohesion between the plies will decrease with the decreasing traction and increasing separation. During this phase, the damage evolution occurs, which describes the degradation of the cohesive stiffness between the plies. Here, the mixed-mode energy release rates are used to describe the dependency of the fracture modes (mode I: opening, mode II: in-plane shear, mode III: out-of-plane shear) so that

$$\left(\frac{G_{\mathrm{I}}}{G_{\mathrm{IC}}} \right) + \left(\frac{G_{\mathrm{II}}}{G_{\mathrm{IIC}}} \right) + \left(\frac{G_{\mathrm{III}}}{G_{\mathrm{IIIC}}} \right) \geq 1. \tag{9}$$

Here, $G_{\mathrm{I}}, G_{\mathrm{II}}, G_{\mathrm{III}}$ are the energy release rates under the modes I, II, and III, respectively while $G_{\mathrm{IC}}, G_{\mathrm{IIC}}, G_{\mathrm{IIIC}}$ are the interlaminar fracture toughnesses. Since the present numerical simulations focus on the low-speed impact, the strain rate effect for the material constants is neglected.

2.2. Statically equivalent impact case based on multi-scale indentation mechanics

During a projectile impact process without penetration, the maximum impact load $P_{\max}$ is achieved at the relative zero speed of the projectile and the target (Andrews et al., 2001), and it can be determined by the impact energy of the projectile W and the impact contact stiffness C_{IP} between the projectile and the target so that (Xu et al, 2018)

$$P_{\max} = \lambda \sqrt[5]{W^3 C_{\mathrm{IP}}^2} \ . \tag{10}$$

Here, λ is a simplified coefficient which includes several factors of the projectile sharpness, boundary and support conditions. In the present study, λ was taken to be 0.38 because the same composite laminates (only stacking sequences are different) with the same impact conditions were used. C_{IP} is calculated for a hemi-spherical indenter/projectile based on Hertz's law and expressed as (Fischer-Cripps, 2011)

$$C_{\mathrm{IP}} = \frac{4}{3}\sqrt{R_{\mathrm{IP}}}E_{\mathrm{r}}, \tag{11}$$

where R_{IP} refers to the radius of the tupper or projectile, and E_{r} is the reduced modulus and determined using the through thickness Young's modulus of the composite laminate E_{33}, which can be obtained from the literature or measured from composite nano-indentation tests, and E_{i} and v_{i} are the Young's modulus and the Poisson's ratio of the tupper, respectively, as (Daniel and Ishai, 2006; Martinez and Xu, 2018)

$$\frac{1}{E_r} \approx \frac{1-v_i^2}{E_i} + \frac{1}{E_{33}}. \tag{12}$$

In the current statically equivalent simulations, the equivalent maximum impact load $P_{\max}$ was directly applied on the composite laminate, and impact damage was predicted. The proposed efficient approach highlights the local dynamic indentation effect and ignores the global bending/shear deformation during impact process. This approach is similar to a common mechanics of material approach to calculate the maximum impact stress of a slender beam subjected to a projectile impact (one-point impact). When the projectile speed is zero, the kinetic energy of the projectile is fully converted to the strain energy (potential energy), and a statically equivalent maximum force is obtained for the impact case (Beer and Johnston, 2014). The maximum impact stress can be easily calculated using classical beam theory. Obviously, the local dynamic indentation, which is a problem of elasticity theory, is ignored for the mechanics of material approach.

2.3. Experimental and numerical simulation procedures

The experiments were conducted with the composite panels composed of IM7/977-3 carbon fiber-epoxy system, the material properties of which are listed in Table 1. The panels had four different stacking sequences, Panel A $[-45/90/45/90/-45/0/45/90/90/-45/90/45]_s$, Panel B $[-45/45/-45/45/0/45/90/-45/45/-45/45/-45]_s$, Panel C $[-45_3/90_3/45_3/0_3]_s$ and Panel D $[-45/90/45/0]_{3s}$, consisting 24 plies each. The panel dimensions were 101.6mm (width), 152.4 mm (length) and 3.2 mm (thickness) according to ASTM standard 7136 for composite impact experiments (Flores et al., 2017). All panels were tested under the impact energy of 5 J. Before the experiments, all the specimens were C-scanned to determine if there were any initial damage defects. During the experiments, composite specimens were clamped onto a fixture with a round hole of 76.2 mm diameter. This impact fixture was fixed to a steel base inside a drop weight tower. The impact event was introduced using a DYNATUP drop-weight tower with a 15.9 mm (5/8 inch) diameter

hemispherical tupper (mass of 3.37 kg). Each impact (impact energy of 5 J) occurred in the center of the specimen, which generated enough energy to create internal damage.

In line with these experiments, the numerical simulations were carried out to simulate impact tests with impact energy of 5 J (current experiments) and 10 J (previous experiments from the literature (Flores et al., 2017)). Based on the stacking sequences of the four panels, local coordinate systems were assigned to each ply. The solution domain for the composite laminates was discretized with 22882 C3D8R linear hexahedral elements with reduced integration, i.e. one integration point per element. The main selection criteria for the reduced integration were to decrease the computational cost and prevent shear or volumetric locking, which is the case for first-order fully integrated elements subjected to bending (Flanagan and Belytschko, 1981). However, for the elements, it is likely that severe mesh distortions may exist despite the strain at the integration point is arbitrarily small or zero, which is known as hourglass effect. In order to prevent such uncontrolled deformations, default hourglass control provided in Abaqus/Explicit was used, i.e. relax stiffness method using the integral visco-elastic form defining anti-hourglass forces (Haddag et al., 2010).

For each simulation case, full scale models were used due to non-symmetric damage evolution observed in the previous experimental studies. Different from the cohesive element utilization, general contact interactions, which uses tracking algorithms to ensure proper contact conditions to all existing interfaces, were applied based on the cohesive behavior of Equations (8) and (9). For two different impact tests with different impact energy and same specimens, the diameters and mass of two steel hemispherical tuppers were 1) 15.9 mm and 3.37 kg for 5 J impact energy test, and 2) 12.7 mm diameter and 5.439 kg for 10 J impact energy tests. Tuppers in both cases were modelled with R3D4 rigid quadrilateral elements. Distance of 0.2 mm was set between the tupper and panel surfaces in order to prevent sudden displacement jumps in the initial simulation configuration. Boundary conditions were defined so that all the translational degrees of freedom were set as zero to reproduce the experimental setup conditions.

Two types of numerical simulations, which were dynamic and statically equivalent simulations, were conducted in the scheme of explicit central-difference time integration by means of Abaqus/Explicit and VUMAT user subroutine. For each time step, the strain increment was used as the input of the constitutive material model coded in the subroutine and stress and corresponding damage states were obtained. In case of the intra- and interlaminar damage criteria of Equations (3),(8) and (9) were reached, stresses at the integration points were computed with reduced stiffness matrices. Due to the large number of increments, all the simulations were run with double precision, for which the length of floating-point variable is 64 bits. The dynamic simulations were mainly used to check the prediction accuracy of the proposed model through the comparison of the simulation and experimental load histories under the impact energy of 5 J. On the other hand, the statically equivalent simulations were used to determine the interlaminar damage (delamination) as a function of the maximum impact load P_{max} obtained from Equation (10). The damaged areas obtained from the simulations were then compared with the experimental values for the impact energy of 10 J (Flores et al., 2017).

Table 1: Mechanical properties of IM7/977-3.

Parameters obtained from the literature		Values
Tensile longitudinal modulus E_{11} (GPa)	(Clay and Knoth, 2017)	164
Tensile transverse modulus E_{22}, E_{33} (GPa)	(Hoos et al., 2017)	8.98
Shear modulus G_{12} (GPa)	(Clay and Knoth, 2017)	5.02
Shear moduli G_{13}, G_{23} (GPa)	(Clay and Knoth, 2017)	3.0
Poisson's ratio v_{12}, v_{13}	(Clay and Knoth, 2017)	0.32
Poisson's ratio v_{23}	(Clay and Knoth, 2017)	0.49
Tensile longitudinal strength X_{1T} (MPa)	(Hoos et al., 2017)	2905
Compressive longitudinal strength X_{1C} (MPa)	(Hoos et al., 2017)	1569
Tensile transverse strength X_{2T} (MPa)	(Hoos et al., 2017)	78.9
Compressive transverse strength X_{2C} (MPa)	(Hoos et al., 2017)	248
Calibrated shear strength X_{1S}, X_{2S} (MPa)		80
Mode I interlaminar fracture toughness G_{IC} (N/mm)	(Clay and Knoth, 2017)	0.256
Mode II/III fracture toughness G_{IIC}, G_{IIIC} (N/mm)	(Clay and Knoth, 2017)	0.649
Interfacial normal strength N (MPa)	(Zhang and Zhang, 2015)	68
Calibrated interfacial shear strengths S, T (MPa)		60

3. RESULTS AND DISCUSSIONS

3.1. Dynamic response and damage of composite laminates subjected to impact (energy 5J)

In order to validate the composite damage model, dynamic simulations were designed in accordance with the impact experiments (impact energy 5 J) for a total time period of t=5 ms, for which the initial tupper velocity was 1.72 m/s. For each time step, the contact forces between the tupper and the panel surfaces were computed and the load histories for each panel were generated and compared with the experimental data as represented in Figure 1. It is noticed that our experimental curves are highly repeatable, because all curves look like one curve. The average experimental peak loads for panels A, B, C, and D were obtained as 3.76 kN, 3.96 kN, 3.27 kN, and 3.89 kN as listed in Table 2. The time to reach the maximum impact force was around 1.5 ms

for all three panels except panel C. The comparative study showed that the simulated load histories had similar trends with the experimental ones. However, the simulated peak loads were deduced to be higher than the measured values, i.e. 4.51 kN, 4.88 kN, 3.98 kN and 4.47 kN, respectively, within a range of 13-19%. In contrast to the peak loads, maximum simulated tupper displacements were less than the experimental ones except Panel D. The percent differences were obtained as 8%, 0.5%, 20% and 9%, respectively. These discrepancies are believed to be due to the inaccuracies in the material constants used in the simulations, e.g., the interlaminar shear strengths *S* and *T*, which were not directly measured and modified from the literature (Zhang and Zhang, 2015).

It is also noteworthy that after the onset of tupper-panel contact, the kinetic energy of the tupper was gradually transferred to the panels as the strain energy, damage initiation and propagation, and vibrations as captured in the load history plots. It was observed that there were large load fluctuations in both simulations and experiments especially before the load reached its peak value. This behavior was mainly caused by the combined effects of both intra- and interlaminar damage initiation and evolution and strong vibrations in the initial tupper-panel contact (Flores et al., 2017; Zhang et al., 2017). After the load reached its peak value, the strain energy of the panel enforced the tupper to bounce back, which is shown in the sequences t=3 ms and t=4 ms of the interlaminar damage evolution of Figure 1. In the recovery period, the impact load gradually decreased, but the damage still existed inside the panels. However, we do not have the measured damage size, so we cannot make a direct comparison. The information from this simulation shows that internal impact damage exists even for very low impact energy (5J), and the damage size is comparable with the tupper size.

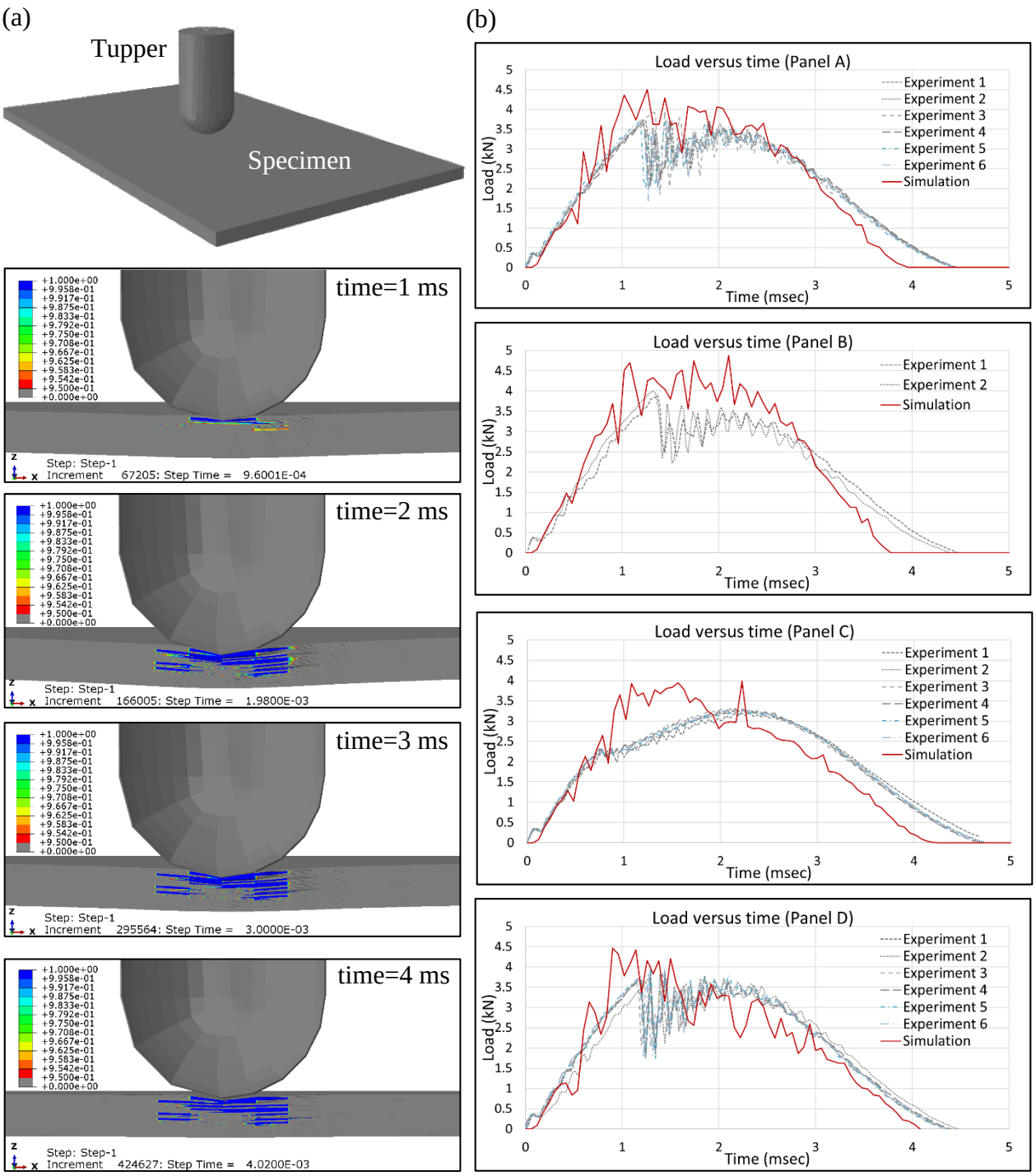

Figure 1: Panels subjected to impact energy of 5 J: (a) simulation setup and half-cut showing the simulated interlaminar damage evolution of Panel A (legend bar shows the interlaminar damage, where elements with blue color (1) refers to completed failed/damaged elements and other color mappings refer to partially damaged or undamaged elements (grey)), (b) impact load history comparison from experiments and numerical simulations of panels A-D.

Table 2: Tupper displacements and peak loads under 5 J.

Panel	Maximum tupper displacement (mm)		Peak load (N)	
	Simulations	Experiments	Simulations	Experiments
A	1.86	2.03 ± 0.02	4506	3758 ± 100
B	1.99	2.00 ± 0.05	4875	3948 ± 71
C	2.06	2.60 ± 0.07	3984	3267 ± 45
D	1.85	1.68 ± 0.13	4469	3374± 171

3.2. Maximum damage comparison of the statically equivalent simulations and impact experiments (energy 10 J)

Our statically equivalent impact simulations are compared with previous experiments of the same composite panels subjected to 10 J impact energy (Flores et al., 2017). In this case, P_{max}~5700 N was used as the input following Equation (10) for the simulations with a total time period of t=2000 ms. As it can be deduced from Figure 2, interlaminar damage evolution had arbitrarily small deviations, which implies that the ratio between the kinetic energy and the potential energy is almost negligible and was well captured in the present statically equivalent simulations.

Based on the present and previous experiments, the interlaminar damage was observed to be critical and causing local instabilities in the panels (Flores et al., 2017; Zhang et al., 2017). In consideration to its importance, maximum values of the simulated and experimental interlaminar damaged areas were compared and presented in Figure 2. For the damaged area representations, the nodal coordinates of the failed elements *crd* with the set size of *N* were extracted from the simulations and fitted to the convex hull formulated as (Weisstein, 2006)

$$C = \left\{ \sum_{j=1}^{N} \lambda_j crd_j : \lambda_j \geq 0 \ \forall \ j \text{ and } \sum_{j=1}^{N} \lambda_j = 1 \right\}. \quad (13)$$

Thereafter, the damaged area was expressed as a planar non-self-intersecting polygon area (Beyer, 1987). In respect to the damaged areas listed in Table 3, it can be deduced that panels A, B and D have 20-30% larger simulated damaged areas than the measured areas. A similar trend was observed in the maximum tupper displacements, resulting in 4-17% difference. These difference were expected because only indentation deformation and energy were considered in the statically equivalent simulations, while bending deformation was not included in order to quickly simulate the maximum damage. Indeed, a large simulated damage area is helpful for conservative damage tolerance design especially in the early composite design stage. For panel C, a large discrepancy between the simulated and measured damaged areas exists due to its small bending stiffness (or large bending deformation) of this particular stacking sequence, which was observed by Flores et

al. (2017). Based on previous studies, the stacking sequence of a composite laminate made important contributions to its damage and failure (Abrate, 1991; Xu, 1995). Therefore, its impact peak load and maximum damaged area were different from the other composite panels. It is noteworthy that almost all aerospace composite structures have large bending stiffnesses or small bending deformation, which is in line with the present numerical simulations. Therefore, the proposed statically equivalent simulation could become a promising and efficient tool for composite damage tolerance designs.

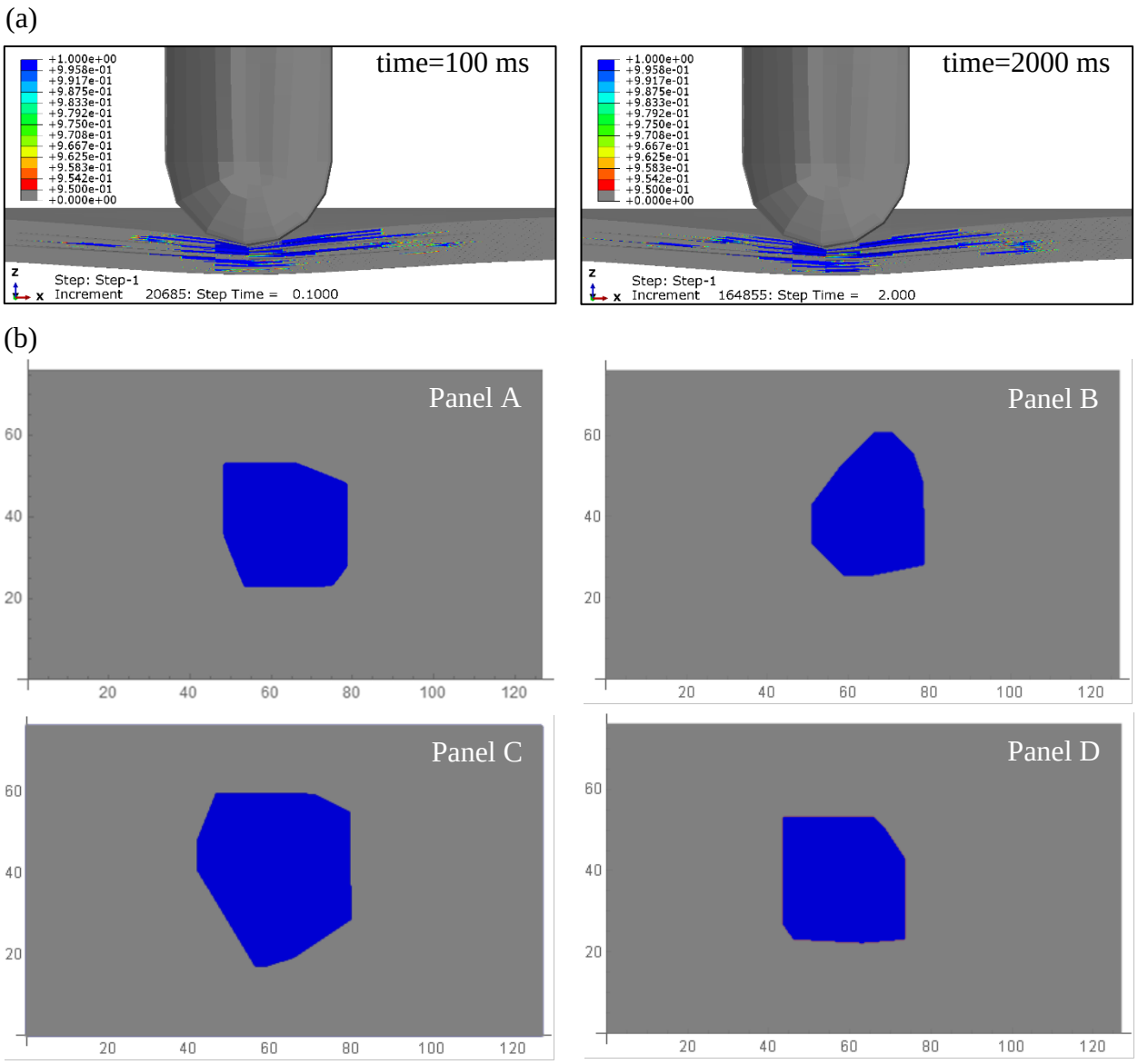

Figure 2: Panels subjected to impact energy of 10 J: (a) half-cut showing the simulated interlaminar damage evolution of Panel A under P_{max}~5700 N (legend bar shows the interlaminar damage, where elements with blue color (1) refers to failed elements and other color mappings refer to partially- or un- damaged elements), (b) simulated overlapping damaged areas for panels A-D (through convex hull fit to the interlaminar damage data extracted from the failed elements in the entire panel solution domain).

Table 3: Tupper displacements and the maximum interlaminar damaged areas (10 J impact energy).

Panel	Maximum interlaminar damaged area (mm^2)		Maximum tupper displacement (mm)	
	Simulations	Literature (Flores et al., 2017)	Simulations	Literature (Flores et al., 2017)
A	824.0	704.9 ± 82.4	4.08	3.57
B	761.6	571.4 ± 73.6	3.89	3.65
C	1432.7	2545.4 ± 363.4	3.69	3.84
D	874.4	704.9 ± 87.9	4.28	3.58

4. CONCLUSIONS

The present study introduces a new simulation approach combining indentation mechanics and computational mechanics to predict the impact behaviors of composite laminates subject to low impact energy (5 and 10 J). The proposed statically equivalent simulation was validated by means of low-speed impact experiments and numerical simulations of composite panels with four different stacking sequences. The simulated impact load history, maximum damage areas, average peak loads and displacements of composite panels with large bending stiffness (panel A, B and D) were in generally good agreement with the measurements. Some discrepancies between the simulation results and experimental measurements are mainly caused by a few inaccurate material constants which were not directly measured and obtained from the literature. Large discrepancy of the simulated and the measured maximum damage area of panel C resulted from the exclusion of bending deformation in the proposed simulation. Due to the same exclusion, the simulated maximum damage areas of panel A, B and D are larger than the measured areas. However, relatively large simulated damage areas are helpful for conservative damage tolerance design. The exclusion of bending deformation is reasonable because almost all aerospace composite structures have large bending stiffnesses or small bending deformation. Eventually, the proposed approach will provide simplified, yet conservative upper-bound estimates for damage and failure of composite laminates.

ACKNOWLEDGMENTS

The authors acknowledge the support from the Air Force Office of Scientific Research (grant number FA9550-18-1-0006, Dr. Jaimie Tiley, Program Officer).

REFERENCES

ABAQUS (2009). *Lecture Notes "Analysis of Composite Materials with ABAQUS."*. Dassault Systemes.

Abrate, S (1991). "Impact on laminated composites materials." *Appl Mech* 44 (4).

Andrews, EW, AE Giannakopoulos, E Plisson, and S Suresh (2001). "Analysis of the impact of a sharp indenter." *International Journal of Solids and Structures* 39: 281-295.

ASTM D7136 D7136M-15 (2015). *Standard Test Method for Measuring the Damage Resistance of a Fiber-Reinforced Polymer Matrix Composite to a Drop-Weight Impact Event.* West Conshohocken, PA: ASTM International

Beer, F, and ER Johnston (2014) *Mechanics of Materials.* New York: McGraw-Hill.

Beyer, WH (1987). *CRC Standard Mathematical Tables*. Boca Raton, FL: CRC Press.

Choi HY, Wu HT, Chang FK (1991). A new approach toward understanding damage mechanisms and mechanics of laminated composites due to low-velocity impact: Part II-analysis. *J. Composite Materials*, 25: 1012-1038

Clay, SB, and PM Knoth (2017). "Experimental results of quasi-static testing for calibration and validation of composite progressive damage analysis methods." *Journal of Composite Materials* (51): 1333-1353.

Daniel, I, and O Ishai (2006). *Engineering mechanics of composite materials.* London, England: Oxford University Press.

Fischer-Cripps, AC (2011). *Nanoindentation*, New South Wales, Australia: Springer Publisher.

Flanagan, DP, and T Belytschko (1981). A uniform strain hexahedron and quadrilateral with orthogonal hourglass control". *International Journal of Numerical Methods in Engineering* (17): 679-706.

Flores, M, DH Mollenhauer, V Runatunga, T Beberniss, D Rapking, and M Pankow (2017). "High-speed 3D digital image correlation of low-velocity impacts on composite plates." *Composites Part B* (131): 153-164.

Geubelle PH, Baylor JS (1998) Impact-induced delamination of composites: a 2D simulation. *Composites Part B* 29B: 589-602.

Haddag, B, S Atlati, M Nouari, M Znasni (2010). "Finite element formulation effect in three-dimensional modeling of a chip formation during machining." International Journal of Material Forming (3): 527-530.

Hoos, K, EV Iarve, M Braginsky, E Zhou, and DH Mollenhauer (2017). "Static strength prediction in laminated composites by using discrete damage modeling." *Journal of Composite Materials* (51): 1473-1492.

Karbhari VM, Rydin RW (1999). Impact characterization of RTM composites—II: damage mechanisms and damage evolution in plain weaves. J. Mater. Sci., 34, 5641–5648.

Lambros J, Rosakis AJ (1997). An experimental study of the dynamic delamination of thick fiber reinforced polymeric matrix composite laminates. *Experimental Mechanics*, 37: 360-366.

Martinez, R, and LR Xu (2018). "Approximate Measurements of the Through-Thickness Young's Moduli of Fibrous Composite Laminates using Nanoindentation." (Submitted).

Nie, Z (2014). *Advanced Mesomechanical Modeling of Triaxially Braided Composites for Dynamic Impact Analysis with Failure, PhD. Thesis.* OH, USA.: University of Akron.

Rhymer J, Kim H, Roach D (2012). The damage resistance of quasi-isotropic carbon/epoxy composite tape laminates impacted by high velocity ice. Composites A, 43: 1134-1144.

Sepe, R, A De Luca, G Lamanna, and Caputo F (2016). "Numerical and experimental investigation of residual strength of a LVI damaged CFRP omega stiffened panel with a cut-out." *Compos Part B Eng J* 102: 38-56.

Singh, H, M Gupta, and P Mahajan (2017). "Reduced order multiscale modeling of fiber reinforced polymer composites including plasticity and damage." *Mechanics of Materials* 111 (35-56).

Sun CT, Rechak S (1988). Effect of adhesive layers on impact damage in composite laminates," In: Whitcomb JD, editor. Composite materials: Testing and Design (8th Conf.), ASTM STP 972, American Society for Testing and Materials, Philadelphia, 97-123.

Weisstein, EW (2006). "Convex Hull." *From MathWorld--A Wolfram Web Resource*.

Xu LY, (1995), Influence of stacking sequence on the transverse matrix cracking in continuous fiber crossply laminates. Journal of composite materials 29:1337-1358

Xu, LR, et al, (2018). " Multi-time/length-scale relations of indentation mechanics for predicting low-speed impact responses of polymers and polymeric composites. " (Submitted).

Xu LR, Rosakis AJ (2002). Impact failure characteristics in sandwich structures:: P art I: Basic failure mode selection." International journal of solids and structures, 39: 4215-4235.

Xu LR, A Krishnan, H Ning, U Vaidya (2012). A seawater tank approach to evaluate the dynamic failure and durability of E-glass/vinyl ester marine composites. Composites Part B: 43:2480-2486

Yaghoub AS, Liaw B (2012). Thickness influence on ballistic impact behaviors of GLARE 5 fiber-metal laminated beams: Experimental and numerical studies. Comp. Struct., 94: 2585-2598.

Yan H, Oskay C, Krishnan A, Xu LR (2010). Compression After Impact Response of Woven Fiber-Reinforced Composites. Composites Science and Technology, 70: 2128-2136

Zhang, C, EA Duodu, J Gu (2017). "Finite element modeling of damage development in cross-ply composite laminates subjected to low velocity impact." *Composite Structures* (173): 219-227.

Zhang, J, and X Zhang (2015). "An efficient approach for predicting low-velocity impact force and damage in composite laminates." *Composite Structures* (130): 85-94.

Measurements of the Approximate Through-Thickness Young's Moduli of Fibrous Composite Laminates using Nanoindentation

Ricardo Martinez[1] and L. Roy Xu[2] *

[1]Department of Mechanical Engineering, University of Texas, El Paso, TX 79968, USA

[2]Department of Mechanical Engineering, University of New Mexico, Albuquerque, NM 87131, USA

ABSTRACT

A new approach of measuring the through-thickness Young's moduli of composite materials using nanoindentation was proposed. First, an approximate expression of the reduced modulus of nanoindentation was introduced for orthotropic composites. Second, nanoindentation was conducted for a glass fiber composite material (E-glass fiber/Vinyl Ester), and the measured Young's modulus was quite consistent with the previously reported value for a similar material system (difference 6.6%). The feature of the proposed nanoindentation approach is its in-service Young's modulus measurements of composites as a function of service time.

Keywords: *Laminate mechanics; Polymer-matrix composites; Mechanical properties; Nanoindentation*

1. Introduction

In mechanics of materials, the Young's moduli are the slopes of the linear parts in stress/strain curves under elastic deformation. Usually large specimens (at least several millimeters) are subjected to uniform tensile load, and their global deformation is measured to obtain the Young's moduli. However, for very small materials or devices such as thin films/coatings, interfaces, or nanocomposites [1-4], this mechanics of material approach is not applicable. So, nanoindentation is almost the only way to measure the Young's moduli [5-6]. Unlike the mechanics of material approach, the indentation approach leads to very complicated three-dimensional, rather than uniform deformation and stress fields [7-26]. Therefore, the Young's moduli measured from nanoindentation are different from the Young's moduli measured from the mechanics of material approach. Unlike the strength of a material, which is determined by its local defects and stress fields, stiffness such as the Young's modulus is a global parameter which represents the average stress and strain effects over one specific material volume such as the gauge length [21]. During the nanoindentation process, this material volume is very small, and its stress and strain fields are

*Phone 1-915-342-0700, Electronic mail: luoyu.r.xu@gmail.com

highly non-uniform compared to a large bar specimen with the uniform stress and strain fields. Therefore, we should treat the Young's modulus measured from nanoindentation as the approximate Young's modulus.

For a composite laminate, its in-plane Young's moduli can be measured using large specimens loaded at a regular material test machine. However, it is not easy to measure the through-thickness Young's modulus. Previous approaches to measure the through-thickness Young's modulus employed complicated specimens such as the through-thickness waisted block specimen, and no test standard was widely accepted [21]. Recently, nanoindentation becomes a convenient tool for the Young's modulus measurements, and its loading direction could be along the thickness direction of a composite laminate. Therefore, nanoindentation can become a viable option for measuring the through-thickness Young's modulus. A main feature of the proposed nanoindentation approach is that it can be employed to measure the in-service Young's modulus, or the Young's modulus as a function of service time. For example, if we want to measure the through-thickness Young's modulus reduction of a large composite panel of an aircraft after five-year service, then some small specimens will be cut from the panel for nanoindentation tests. Based on two extensive review papers on composite nanoindentation, our proposed approach is unique [13, 25]. Hence, the objective of this investigation is to develop a new nanoindentation approach to measure the composite through-thickness Young's modulus based on indentation and composite mechanics theory. We start to address some theoretical issues first.

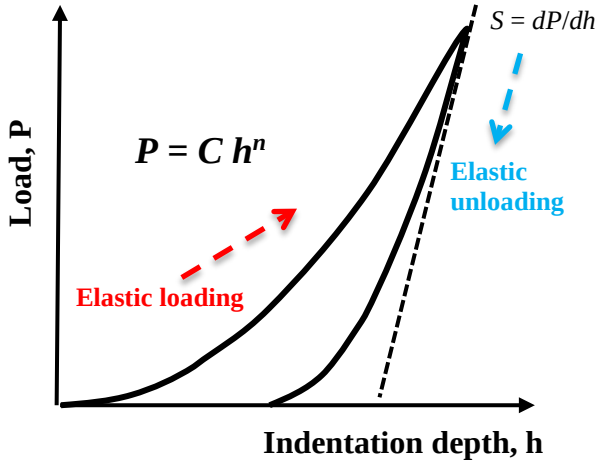

Figure 1. *A typical load-displacement curve for a nanoindentation process.*

2. Indentation mechanics on the composite Young's modulus measurements

As shown in Figure 1, Hertz's contact law is only applicable to the initial elastic loading stage. The indentation load P of a spherical indenter is a function of the indentation depth h and the indenter radius R based on Hertz's contact law [22]:

$$P = Ch^{\frac{3}{2}} = \frac{4}{3}\sqrt{R}E_r h^{\frac{3}{2}} \quad (1)$$

where C is the contact stiffness. The reduced modulus E_r is determined by the Young's modulus E and the Poisson's ratio v of the indenter material and the test material. If they are isotropic and homogeneous materials then,

$$\frac{1}{E_r} = \frac{1-\nu_i^2}{E_i} + \frac{1-\nu^2}{E} \tag{2}$$

where the subscript i refers to the indenter. After the reduced modulus is obtained, the Young's modulus of the test material E could be calculated using equation (2) if other elastic constants are known. In a classical paper by Oliver and Pharr [23], they employed the initial elastic unloading slope of the load/displacement curve dP/dh (Figure 1) to obtain the reduced modulus:

$$\frac{dP}{dh} = \frac{2}{\sqrt{\pi}}\sqrt{A_C}E_r \tag{3}$$

where the contact area A_c is obtained using an estimation procedure. Oliver and Pharr's procedure is widely used to analyze the nanoindentation results of metals and ceramics [24]. But their procedure for polymer indentation application was difficult as the Young's moduli were commonly overestimated because of the viscoelastic effects and pileup [25-26]. We believe that equation (3) is not a reasonable assumption for composite indentation, because large plastic deformation and complicated local damage occur after a deep indentation. Therefore, an elastic unloading stage may not exit, and the contact area A_c is not accurate too (not direct measurement). In this paper, we will use Hertz's contact law (initial elastic loading curve as shown in Figure 1) to fit the Young's moduli because the initial loading stage is easy to control. As a comparison, nanoindentation experiments to measure the same through-thickness Young's moduli using Oliver and Pharr's approach (elastic unloading curve) by other researchers will be presented.

For indentation on fibrous composite laminates, equation (2) should be modified based on Willis' pioneering work [7]. He found that Hertz's contact law (i.e., equation (1)) was still applicable to transversely isotropic composite laminates (a kind of orthotropic laminates). For most fibrous composite applications, woven-fabric composite laminates or other orthotropic laminates, are widely used in modern structures as shown in Figure 2. In order to address the orthotropic properties of composite materials during indentation, a new expression for the reduced modulus should be proposed. Here we assume that Hertz's contact law is still applicable to the orthotropic composite laminates. If orthotropic composites are subjected to normal strain, shear strain will not occur or their deformation is symmetrical. As shown in Figure 2(b), a square composite unit deforms into a rectangular unit if it is subjected to compressive indentation load, or only normal strains exist during deformation. Then, these composites have so-called "orthotropic" properties. Another possible unit deformation is shown in Figure 2(c), i.e., the final unit shape becomes distorted due to coupled normal and shear strains (anisotropic properties). Obviously, deformation in Figure 2(b) is symmetrical but deformation in Figure 2(c) is not at all. It is very important for the indenter to indent the material in a symmetrical way such that we can measure the meaningful mechanical properties. Furthermore, we found from our previous high-speed photography that a through-thickness dynamic indentation (or out-of-plane impact) process of a composite/sandwich specimen was perfectly symmetrical during dynamic crack propagation process [27-28]. Moreover, our in-situ photo-elasticity images also showed that a static indentation deformation of

a model fiber pushout experiment for fibrous composite materials was quite symmetrical [29]. Therefore, we can get simplified relations to characterize the indentation experiments of orthotropic composite laminates. We notice that the second term of equation (2) is for the indenter material only, so it will not change for composites indentation. But the third term is related to the test material (composite materials) and should be modified.

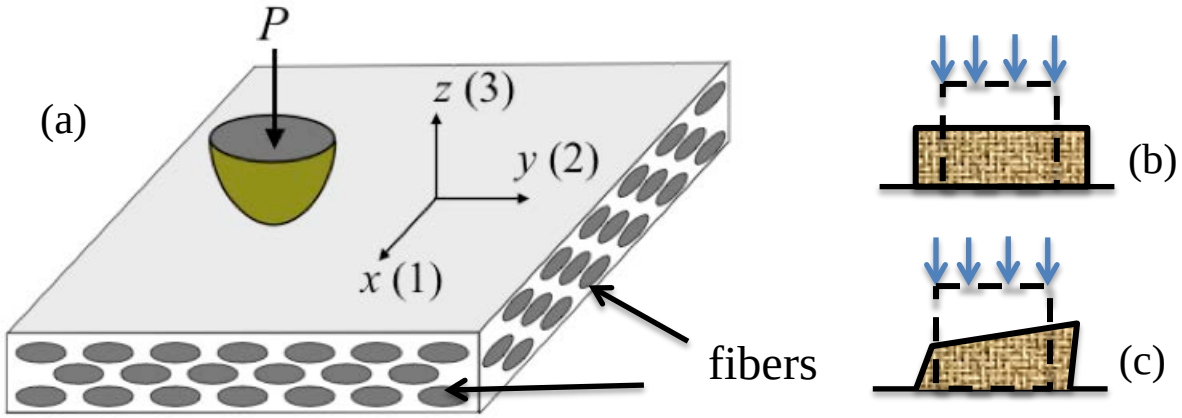

Figure 2*. (a) Nanoindentation along the thickness direction (z or 3-direction) of a woven-fabric composite laminate, (b) orthotropic laminates have normal strains only or symmetrical deformation, (c) anisotropic laminates have coupled normal and shear deformation and their deformation is not symmetrical.*

In a material coordinate system 1-2-3 for fibrous composite laminates, 1 (or x) refers to the major fiber direction, 2 (or y) refers to the transverse in-plane direction, or the minor fiber direction (less fibers compared to 1-direction), and 3 (or z) refers to the thickness direction. Because the indenter is perpendicular to the composite laminate, the measured Young's modulus is the through-thickness Young's modulus E_{33}, which replaces E of equation (2). When indentation force is applied along the 3-direction, it leads to normal deformation/strains along the 1 and 2-directions, so two major Poisson's ratios v_{31} *and* v_{32} should be included in the third term. Such an analysis is analogous to Hertz's classical derivation of a three-dimensional deformation state of indentation of an isotropic and homogenous material [9], because his original contact mechanics analysis which included the Poisson's effects along the x and y directions led to classical equations (1) and (2). A major challenge of composite nanoindentation to measure the Young's moduli is that a simple and exact expression similar to equation (2) is still not available [10-12]. However, we can use two Poisson's ratios v_{31} *and* v_{32} to replace the Poisson's ratio in equation (2), so an approximate expression of the reduced modulus is:

$$\frac{1}{E_r} \approx \frac{1-\nu_i^2}{E_i} + \frac{1-\nu_{31}\,\nu_{32}}{E_{33}} \qquad (4)$$

Equation (4) yields to equation (2) if these two Poisson's ratios are replaced by one Poisson's ratio for isotropic and homogenous materials. We notice that there are some relationships between four Poisson's ratios and three Young's moduli of orthotropic composite materials [21]:

$$\frac{\nu_{13}}{E_{11}} = \frac{\nu_{31}}{E_{33}} \ , \ \frac{\nu_{23}}{E_{22}} = \frac{\nu_{32}}{E_{33}} \tag{5}$$

In order to estimate the magnitude of the product of $v_{31}\, v_{32}$ in equation (4), we employed typical material properties for two kinds of orthotropic composite materials, and results were shown in Table I. Because v_{31} and v_{32} of typical glass fiber composites and carbon fiber composites are very small, their product $v_{31}\ v_{32}$ is almost zero. Therefore, we can obtain a very simple approximate expression of the reduced modulus for orthotropic composite indentation:

$$\frac{1}{E_r} \approx \frac{1-\nu_i^2}{E_i} + \frac{1}{E_{33}} \tag{6}$$

Table I. Calculation results of two through-thickness Passion's ratios v_{31} and v_{32} of typical composites and other materials properties

Woven Fabric Composites	*Fiber volume*	E_1 GPa	E_2 GPa	E_3 GPa	v_{12}	v_{23}	v_{13}	v_{31}	v_{32}
E-glass/Epoxy [21, Page 380] (M10E/3783)	50%	24.5	23.8	11.6	0.11	0.20	0.15	***0.07***	***0.097***
E-glass /Vinyl Ester [30] (this study)	54%	29.2	23.9	**12.4**	0.16				
Carbon/Epoxy [21] (AGP370-5H/3501-6S)	62%	77.0	75.0	13.8	0.06	0.37	0.50	***0.09***	***0.068***

Our approximate approach is easy to be implemented. After the reduced modulus is obtained from equation (1) or (3), the through-thickness Young's modulus E_{33} can be estimated using equation (6). In the following session, we plan to use these relations to obtain the approximate through-thickness Young's modulus of a glass-fiber composite laminate. It is noticed that a spherical indenter, rather sharp indenters with different shapes such as a Berkovich indenter, should be employed in composites nanoindentation experiments in order to avoid complicated phenomena. For example, a sharp indenter tip often leads to damage in matrices or interfaces. Moreover, numerical simulations show that plastic deformation occurs under very small indentation load due to the high stress concentration inside the materials around the sharp tips [17,32].

3. Materials and experimental procedures

The composite material system tested was an E-glass fiber/Vinyl Ester (E-glass/VE) composite in the form of plain-woven fabric composites (eight plies and the total laminate thickness is 5mm) using vacuum assisted resin transfer molding. This composite system was used to investigate the durability and dynamic failure properties in our previous studies [30], as it is widely used in ship structures and wind turbines. The fiber volume percent is 54% after burn off testing and some material properties are listed in Table I. Nanoindentation experiments of seven square specimens (10mm x 10mm) were performed using a TI 750 Hysitron Ubi nanoindentation system with a spherical diamond indenter (radius R=200 μm). In order to reduce the

inhomogeneous feature of the composite modulus measurement, we recommend a spherical indenter with a large radius. Nanoindentation was conducted with a separation between two indents of 200 μm along x and y directions in the central area of the specimen. The maximun applied load was 10 mN such that no plastic deformation occurred during the indentation process. The maximum indentation depth was around 150 nm. Our finite element analysis showed that the above indentation deformation was purely elastic [32]. Therefore, a separation between two indents of 200 μm was sufficient, especially indentation deformation was purely elastic (deformation recovers completely). We notice that the average diameter of a glass or carbon fiber was around 10 μm [21], the edge length of a square composite representative volume element (50% fiber volume percent) was around 12.5 μm, and the radius of the spherical indenter is 200 μm, so our results will not be prone to random material inhomogeneity. For example, at the maximum indentation depth, the diameter of the indenter/specimen contact area (close to a circle) is 16 μm (>12.5 μm). Moreover, we also indent at least 150 locations on one composite specimen. The loading segments were defined as ramp functions for loading and unloading [33]. The time spans were six seconds, four seconds and one second for loading, holding and unloading time respectively. A special fitting approach to deal with very small initial deformation from nanoindentation data which was outlined by Fischer-Cripps [22], was employed to determine the effective contact points.

4. Results and discussion

Our experiments showed consistency with the expected elastic loading and unloading behaviors. One typical load/indentation depth curve was presented in Figure 3 (selected data points, not all data points). No creep was developed during holding time, and the unloading path was very close to the loading path to show the pure elastic deformation. Therefore, Hertz's contact law is valid for all experiments. These experimental curves were employed to fit equation (1) and obtain E_r, and then the through-thickness Young's modulus E_{33} was extracted from equation (6).

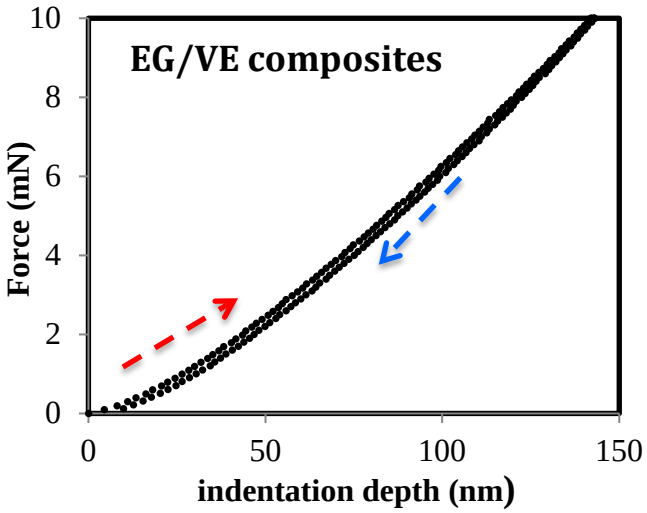

Figure 3. *A typical nanoindentation loading/unloading curve of a composite laminate.*

The average through-thickness Young's modulus was 12.36 ± 3.13 GPa, while the lower bound of this modulus could be predicted by a series rule-of-mixture model [21]. Based on

micromechanics, the lower-bound composite modulus E_{33} is determined by the Young's moduli of the fiber and the matrix E_f and E_m, and the fiber volume percent V_f :

$$\frac{1}{E_{33}} = \frac{V_f}{E_f} + \frac{1-V_f}{E_m} \tag{7}$$

The tensile moduli of the matrix and the fiber of the E-glass/VE composite system are 3.40 GPa and 70.00 GPa respectively [34], so the theoretical lower bound of the composite Young's modulus is 6.85 GPa, which is close to the lowest measured modulus 8.23 GPa. Here, we did not employ other micromechanics approaches such as Halpin-Tsai's semi-empirical equations, since these equations require several fitting parameters, and moreover, they do not provide the theoretical lower bound values which are needed in this investigation.

However, we are not able to make a direct comparison for the measured Young's modulus because we cannot find someone who can make the complicated through-thickness waisted block specimen. So we have to compare the through-thickness Young's moduli of different glass fiber composite systems. Our measured Young's modulus 12.36 GPa is very close to the through-thickness Young's modulus 11.60 GPa of a similar composite material system E-glass/epoxy (M10E/3783) as shown in Table I (6.55% difference). Indeed, two fiber volume percents of the same E-glass fiber of 1) previous E-glass/epoxy composites (V_f =50%) and 2) current E-glass/VE composites (V_f =54%) are very close. Moreover, the Young's modulus of epoxy matrix is 3.80 GPa, which is very close to 3.40 GPa of vinyl ester matrix. Therefore, the through-thickness Young's moduli of these two composite systems (E-glass/epoxy and current E-glass/VE) should be very close. The above results demonstrated that the convenient nanoindentation test can replace the complicated through-thickness waisted block test for the through-thickness Young's modulus measurement.

Meanwhile, the through-thickness Young's modulus of the same E-glass/VE composites was also measured independently by two different laboratories. As preliminary studies, Fischer-Cripps' Lab reported that the Young's modulus was from 5.00 to 7.00 GPa using a spherical diamond indenter (R=100 μm) under the maximum load of 420 mN. The maximum indentation depth was 2.5 μm, and 40 indentations were conducted [31]. CMS Lab found that the Young's modulus was around 7.00 GPa using a diamond Vickers indenter under the maximum load of 2, 000 mN. Loading and unloading rate was 4,000.00 mN/min. The maximum indentation depth was 22.0 μm, and 50 indentations were conducted [35]. They both used Oliver and Pharr's approach to estimate the Young's modulus with an assumed Poisson's ratio ν (=0.30) for composite materials in equation (2). We should convert their results into the correct moduli using equation (6), since the Poisson's ratio ν is not required for composites in this equation. Because E_{33} is around 5.00 to 15.00 GPa, and the Young's modulus of the diamond indenter E_i is at least 1,000.00 GPa, $E_3 \approx E_r$. However, their calculation was based on equation (2), and the corrected Young's modulus ≈ E (their value)/ $(1-\nu^2)$. Therefore, the corrected Young's moduli based on their measurements were from 5.50 to 7.70 GPa, which were quite lower than our measured Young's modulus. But their measurements were still close to the theoretical lower bound 6.85 GPa which was predicted by equation (7). Recently, our investigation on polymer nanoindentation [32] showed that the Young's modulus measurement based on the elastic indentation curve using Hertz's contact law was more accurate than the measurement based on the elastic unloading curve using Oliver and Pharr's approach due to complicated plasticity and damage involved [36]. The current results on composite materials further enhance this conclusion, since the modulus

measurements using Oliver and Pharr's approach were close to the lower bound prediction, while results from our new approach were close to the direct Young's modulus measurements using the waisted block test.

In the recent 15 years, several papers on the nanoindentation tests of composite materials were published [1,20, 37-39]. Their major objective was to measure local material properties using sharp indenters. While the goal of this paper is to measure a global material property—the Young's modulus using a non-sharp indenter. It is important to notice that if the indenter tip is smaller than the reinforcement such as a particle or fiber in composite or other heterogeneous materials, the indentation curves for the particles/fibers and the matrix zones were very different [33, 37]. Moreover, Hardimana et al. found that the measured modulus using nanoindentation was a complicated function of the depth [38]. Although the initial indentation modulus referred to the original matrix modulus, the measured modulus increased sharply when the stiff fiber under the matrix was stressed. Therefore, the Young's modulus which represents the global deformation capability of both the matrix and the reinforcement cannot be measured using a sharp indenter. If we have to employ a sharp indenter to measure the composite modulus, we proposed a new approach based on micromechanics and contact mechanics to estimate the lower bound of the Young's moduli. The lower bound values are valuable for conservative material design based on the safety consideration [40].

5. Conclusion

In summary, a new approach of measuring the through-thickness Young's moduli of orthotropic fibrous composite laminates using convenient nanoindentation is proposed. The measured Young's modulus of a glass fiber composite material was quite consistent with a previous measurement for a similar composite material system. Results show that the measurement based on the elastic loading curve using Hertz's contact law is more accurate than the measurement based on the elastic unloading curve using Oliver and Pharr's approach.

Acknowledgements: The authors acknowledge the support from the US Air Force Office of Scientific Research (grant number FA9550-18-1-0006, Dr. Jaimie Tiley, Program Officer). Valuable discussion and measurement results from Drs. A. Fischer-Cripps, B. Zhou, Z. Zong and P. Borgaonkar are appreciated.

Data availability

The raw/processed data required to reproduce these findings cannot be shared at this time due to technical or time limitations.

Reference

1 Ureña A, Rams J, Escalera M D and Sanchez M 2005, Characterization of interfacial mechanical properties in carbon fiber/aluminum matrix composites by the nanoindentation technique, *Composites Science and Technology,* **65,** 2025– 2038

2 Xu L R, Li L, Lukehart C M and Kuai H 2007 Mechanical Property Characterization Nanofiber-Reinforced Composite Adhesives, *Journal of Nanoscience and Nanotechnology* **7** 2546-2548

3 Wei X and J W Kysar, 2012 Experimental validation of multiscale modeling of indentation of suspended circular graphene membranes *International Journal of Solids and Structures* **49** 3201–3209.

4 Heinrich C, Waas AM, Wineman AS (2009) Determination of material properties using nanoindentation and multiple indenter tips. *International Journal of Solids and Structures* **46** 364-376

5 Cao G, Chen X, Xu Z-H, Li X 2010 Measuring mechanical properties of micro- and nano-fibers embedded in an elastic substrate: Theoretical framework and experiment, *Composites Part B: Engineering* **41** 33-41

6 Lu Y C, Jones D C, Tandon G P, Putthanarat S, Schoeppner G A 2010 High Temperature Nanoindentation of PMR-15 Polyimide, *Experimental Mechanics* **50** 491-49

7 Willis J R 1966 Hertzian contact of anisotropic bodies, *Journal of Mechanics and Physics of Solids* **14** 163–176

8 Muliana, A. H., Steward, R. Haj-Ali, R. H., and Saxena, A., 2002 Artificial Neural Network and Finite Element Modeling of Nano-Indentation Tests. *Metallurgical and Materials Transactions-A*, 33A, 1939-1947.

9 Johnson K L *Contact Mechanics* (Cambridge University Press, Cambridge, England, 1985)

10 Jorgensen O, Giannakopoulos A E, and Suresh S 1998, Spherical indentation of composite laminates with controlled gradients in elastic anisotropy , *International Journal of Solid Structures* **35** 5097–5113

11 Chen W, Pan N, Wang, H Zhang Ch 2010, Theory of indentation on multiferroic composite materials, *Journal of the Mechanics and Physics of Solids* **58** 1524–1551

12 Delafrague A and Ulm F J 2004. Explicit approximations of the indentation modulus of elastically orthotropic solids for conical indenters, *International Journal of Solids and Structures* **41** 7351–7360.

13. Gibson RF, 2014 A review of recent research on nanoindentation of polymer composites and their constituents, *Composites Science and Technology*, **105** 51-65

14 Gao Y F and Pharr G M 2007 Multidimensional contact moduli of elastically anisotropic solids, *Scripta Materialia* **57** 13–16.

15 Ghosh D, Subhash G, Sudarshan T S, Radhakrishnan R and Gao X-L 2007 Dynamic Indentation Response of Fine-Grained Boron Carbide , *Journal of the American Ceramic Society* **90,** 1850-1857

16 Nakamura T and Y Gu 2007 Identification of elastic–plastic anisotropic parameters using instrumented indentation and inverse analysis, *Mechanics of Materials* **39** 340–356

17 Rittel B P, and Ravichandran G 2008 An analysis of nanoindentation in linearly elastic solids , *International Journal of Solids and Structures* **45** 6018–6033

18 Vlassak JJ , M. Ciavarella, J.R. Barber, X. Wang 2003. The indentation modulus of elastically anisotropic materials for indenters of arbitrary shape, *Journal of the Mechanics and Physics of Solids*, **51,** 1701 – 1721

19 Zhou Z and Lu H 2010 On the Measurements of Viscoelastic Functions of a Sphere by Nanoindentation, *Mechanics of Time-Dependent Materials,* **14** 1-24

20 Olivas, E. R. J. G. Swadener and Y.-L. Shen, 2006 Nanoindentation Measurement of Surface Residual Stresses in Particle-Reinforced Metal Matrix Composites, *Scripta Materialia* **54**, 263-268.

21 Daniel I, Ishai O *Engineering mechanics of composite materials* (Oxford University Press, London, England 2006).

22 Fischer-Cripps A C 2011. *Nanoindentation* (Springer Publisher, New South Wales, Australia)

23 Oliver W C and Pharr G M 1992 An improved technique for determining hardness and elastic modulus using load and displacement sensing indentation experiments, *Journal of Materials Research* **7** 1564-1583

24 Jha K K, Suksawang N, Lahiri D. and Agarwal A 2013 Evaluating initial unloading stiffness from elastic work-of-indentation measured in a nanoindentation experiment , *Journal of Materials Research* **28** 789-797

25 Hardimana M. T.J. Vaughanb, C.T. McCarthy. 2017 A review of key developments and pertinent issues in nanoindentation testing of fibre reinforced plastic microstructures, Composite

Structures **180** 782–798

26 Tranchida D, Piccarolo S, Loos J, Alexeev A 2006 Accurately evaluating Young's modulus of polymers through nanoindentations: A phenomenological correction factor to the Oliver and Pharr procedure, *Applied Physics Letters* **89** 171905-171907

27 Xu LR, Rosakis AJ 2002. Impact failure characteristics in sandwich structures: Part I: Basic failure mode selection, *International Journal of Solids and Structures*, **39** 4215-4235.

28. Xu LR, AJ Rosakis 2005. Impact damage visualization of heterogeneous two-layer materials subjected to low-speed impact, *International Journal of Damage Mechanics* **14**, 215-233

29. Xu, LR H Kuai, S Sengupta 2005. Free-edge stress singularities and edge modifications for fiber pushout experiments, *Journal of composite materials* **39,** 1103-1125.

30. Xu L R, A Krishnan, H Ning; U Vaidya, 2010 A seawater tank approach to evaluate the dynamic failure and durability of E-glass/vinyl ester marine composites, *Composite Part B.* **43** 2480–2486

31. Fischer-Cripps A. 2011, private communication.

32 Martinez R. and L. Roy Xu, 2014. Comparison of the Young's Moduli of Polymers Measured from Nanoindentation and Bending Experiments, *MRS communications,* **4**, 89–93

33 Simpson A 2011, Hysitron Inc. Minneapolis, MN, private communication.

34 Yan, H. C. Oskay, A. Krishnan and L.R. Xu, 2010. Compression After Impact Response of Woven Fiber-Reinforced Composites, *Composite Science and Technology,* **70,** 2128-2136

35 Zong Z and P. Borgaonkar, 2011. CSM Instruments, private communication.

36 Gerberich W W, Kramer W Y, Bahr D, Stronjy A, Lilleodden E, and Nelson J, 1997 Elastic loading and elastoplastic unloading from nanometer level indentations for modulus determinations *Journal of Materials Research* **13** 421-439

37. Yedla, S.B. M. Kalukanimuttam, R. M. Winter and S. K. Khanna. 2008. Effect of Shape of the Tip in Determining Interphase Properties in Fiber Reinforced Plastic Composites Using Nanoindentation, *Journal of Engineering Materials and Technology,* **130,** 41010-041025.

38. Hardimana M. T.J. Vaughanb, C.T. McCarthy. 2015. Fibrous composite matrix characterization using nanoindentation: The effect of fibre constraint and the evolution from bulk to in-situ matrix properties. *Composites: Part A,* **68**, 296-303.

39. Gregory JR, Spearing SM. 2005. Nanoindentation of neat and in-situ polymers in polymer–matrix composites. *Compos Sci Technol*; 65:595–607.

40.Xu L. R. Martinez R., Zhao, K. 2018. Micromechanics Characterization on the Lower Bound Young's Moduli of Composite and Heterogeneous Materials Measured from Nanoindentation, submitted for publication.

Micromechanics Characterization on the Lower Bound Young's Moduli of Composite Materials Measured from Nanoindentation

L. R Xu [1] R. Martinez [2], K. Zhao[2]*

[1]Department of Mechanical Engineering, University of New Mexico, Albuquerque, NM 87131, USA

[2]Department of Mechanical Engineering, University of Texas at El Paso, El Paso, TX 79968, USA

ABSTRACT

The measurements of the through-thickness Young's moduli for composite materials are important but they were not systematically reported because of their complexity. In this paper, a lower bound characterization approach for the Young's moduli using elastic nanoindentation unloading curves is proposed based on contact mechanics and micromechanics analysis. This approach was applied to grid nanoindentation of a glass-fiber composite material system, and the estimated lower bound was around 40% lower than the measured Young's modulus of the same composite system using Hertz's contact law and elastic loading curves. Therefore, the proposed approach provides a conservative measurement if the actual through-thickness Young's modulus is not available. This approach is helpful for nanoindentation users without comprehensive knowledge of micromechanics and contact mechanics to deal with complicated indentation for composites or heterogenous materials.

Keywords: *Composite Material; Mechanical Characterization; Micromechanics; Nanoindentation.*

[*] Corresponding author, phone 1-915-342-0700, e-mail: luoyu.r.xu@gmail.com

1. Introduction

Composite materials are widely used in aerospace, civil, marine and other structures such as wind turbine blades and cars. While these materials bear many attractive features, they have one major shortcoming due to their lower impact resistance along their thickness direction. Moreover, potential impact scenarios for composite structures appear to be quite diverse such as birds, tools, hail, and debris. In order to predict impact damage of composite materials, mechanical properties such as the through-thickness Young's moduli should be measured accurately.

For very small materials or devices such as thin films/coatings, interfaces, or nanocomposites [1-4], nanoindentation becomes a convenient tool to measure the Young's moduli [5-6]. However, local indentation leads to very complicated three-dimensional, rather than uniform deformation and stress fields [7-21]. Therefore, the Young's moduli measured from nanoindentation are different from the Young's moduli measured from the mechanics of material approach (large specimens subjected to uniform stress/strain fields). Recently, the authors proposed a new approach of measuring the through-thickness Young's moduli of orthotropic composites laminates, and the measured Young's modulus of one composite system was quite consistent with the previously reported value for a similar material system [22]. The main feature of the new nanoindentation approach was employing Hertz's contact law to obtain the Young's moduli of composite laminates subjected to spherical indentation. However, many nanoindentation users mainly employ sharp indenters and the elastic unloading curves (Figure 1) to obtain the reduced moduli (Oliver and Pharr's approach [23-24]), and the measured moduli vary very differently in different locations due to the heterogeneous nature of composites. For example, Hardimana et al. found that the measured moduli using a sharp indenter were complicated

functions of the indentation depths and locations [19]. Although the initial modulus referred to the matrix modulus, the measured modulus increased sharply when the stiff fiber under the matrix was stressed. Therefore, the Young's modulus which represents the global deformation capability of both the matrix and the reinforcement cannot be measured using a sharp indenter. Obviously, these local measurements are not able to provide the composite modulus, which is a global parameter based on the volume average. In order to employ a sharp indenter to measure the composite moduli, we propose a micromechanics approach to estimate the lower bound of the Young's moduli in this paper. The lower bound values are still valuable for conservative material design based on the safety consideration [21].

2. Two Indentation Approaches for Composite Young's Modulus Characterization

2.1. Composite Young's moduli directly measured from the elastic loading curves

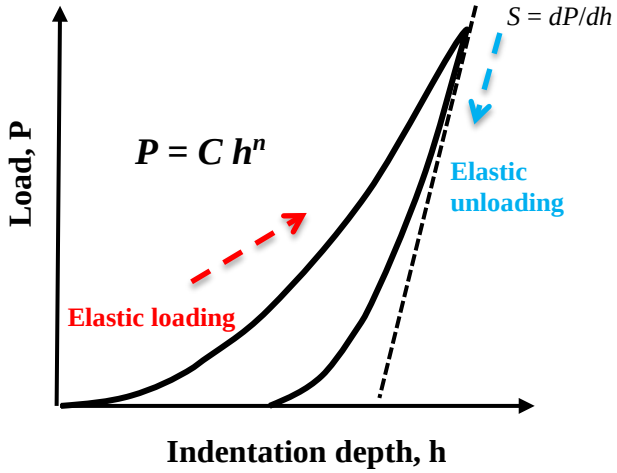

Figure 1. *A typical load-displacement curve for a nanoindentation process.*

As shown in Figure 1, Hertz's contact law is only applicable to the initial elastic loading

stage. The indentation load *P* of a spherical indenter is a function of the indentation depth *h* and the indenter radius *R* based on Hertz's contact law [23]:

$$P = Ch^{\frac{3}{2}} = \frac{4}{3}\sqrt{R}E_r h^{\frac{3}{2}} \quad (1)$$

where C is the contact stiffness. The reduced modulus E_r is determined by the Young's modulus *E* and the Poisson's ratio *v* of the indenter material and the test material. If they are isotropic and homogenous materials, then,

$$\frac{1}{E_r} = \frac{1-\nu_i^2}{E_i} + \frac{1-\nu^2}{E} \quad (2)$$

where the subscript *i* refers to the indenter. After the reduced modulus is obtained, the Young's modulus of the test material *E* could be calculated using equation (2) if other elastic constants are known. In a classical paper by Oliver and Pharr [24], they employed the initial elastic unloading slope of the load/displacement curve *dP/dh* (Figure 1) to obtain the reduced modulus:

$$\frac{dP}{dh} = \frac{2}{\sqrt{\pi}}\sqrt{A_C}E_r \quad (3)$$

where the contact area A_c is obtained using an estimation procedure. Oliver and Pharr's procedure is widely used to analyze the nanoindentation results of metals and ceramics [24]. But their procedure for polymer indentation was difficult as the Young's moduli were commonly overestimated because of the viscoelastic effects and pileup [25-26].

For indentation on fibrous composite laminates, equation (2) should be modified based on Willis' pioneering work [7]. He found that Hertz's contact law (i.e., equation (1)) was still applicable to transversely isotropic composite laminates (a kind of orthotropic laminates). For most fibrous composite applications, woven-fabric composite laminates or other orthotropic laminates,

are widely used in modern structures as shown in Figure 2. To address the orthotropic properties of composite materials during indentation, a new expression for the reduced modulus should be proposed. Here we assume that Hertz's contact law is still applicable to the orthotropic composite laminate, i.e., applied normal strain would not lead to the shear strain. As shown in Figure 2(b), a square composite unit deforms into a rectangular unit if it is subjected to compressive indentation load, or only normal strains exist during deformation. Then, these composites have so-called "orthotropic" properties. Another possible unit deformation is shown in Figure 2(c), i.e., the final unit shape becomes complicated due to coupled normal and shear strains (anisotropic properties). Obviously, deformation in Figure 2(b) is symmetrical but deformation in Figure(c) is not at all. Furthermore, we found from high-speed photography that a through-thickness dynamic indentation (or out-of-plane impact) process of a composite/sandwich specimen was perfectly symmetrical during dynamic crack propagation process [27-28]. Therefore, we can get simplified relations to characterize the indentation of orthotropic composite laminates. We notice that the second term of equation (2) is for the indenter material only, so it will not change for composites indentation. But the third term is related to the test material (composite materials) and should be modified.

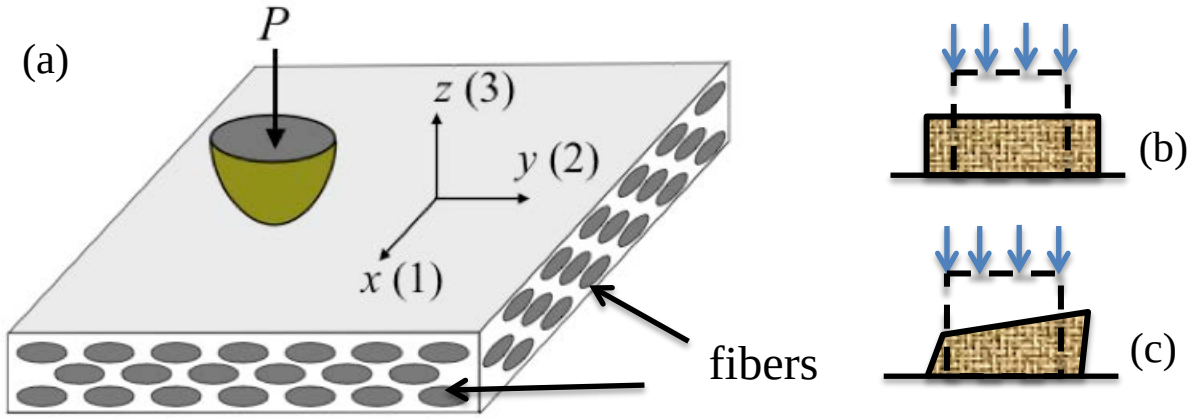

Figure 2*. Nanoindentation along the thickness direction (z or 3-direction) of a woven-fabric composite laminate (a), orthotropic laminates have normal strains only under compressive indentation load (b), and anisotropic laminates have coupled normal and shear deformation under the same compressive load (c)*

In a material coordinate system 1-2-3 for fibrous composite laminates, 1 (or x) refers to the major fiber direction, 2 (or y) refers to the transverse in-plane direction, or the minor fiber direction (fewer fibers compared to 1-direction), and 3 (or z) refers to the thickness direction. Because the indenter is perpendicular to the composite laminate, the measured Young's modulus is the through-thickness Young's modulus E_{33} (or E_z) which replaces E of equation (2). When indentation force is applied along the 3-direction, it leads to through-thickness normal deformation (no shear deformation) along the 1 and 2-directions, so two major Poisson's ratios v_{31} *and* v_{32} should be included in the third term. Such an analysis is analogous to Hertz's classical derivation of a three-dimensional deformation state of indentation of an isotropic and homogeneous material [11], because his original contact mechanics analysis which included the Poisson's effects along the x and y directions led to classical equations (1) and (2). A major challenge of composite nanoindentation to measure the Young's moduli is that an exact expression similar to equation (2) could be very complicated and is still not available. However, we can use two Poisson's ratios v_{31}

and v_{32} to replace the Poisson's ratio in equation (2), so an approximate expression of the reduced modulus is:

$$\frac{1}{E_r} \approx \frac{1-\nu_i^2}{E_i} + \frac{1-\nu_{31}\,\nu_{32}}{E_{33}} \approx \frac{1-\nu_i^2}{E_i} + \frac{1}{E_{33}} \tag{4}$$

Equation (4) yields to equation (2) if these two Poisson's ratios v_{31} *and* v_{32} are replaced by one Poisson's ratio for isotropic and homogeneous materials. To estimate the magnitude of the product of $v_{31}\,v_{32}$ in equation (4), we employ typical material properties of orthotropic composite materials [21] and find it is almost zero. Therefore, we can obtain a very simple expression of the reduced modulus for orthotropic composite indentation as shown in equation (4). The proposed approximate approach by Martinez and Xu is easy to be implemented [22]. After the reduced modulus is obtained from equation (1), the through-thickness Young's modulus E_{33} can be estimated using equation (4). It should be noticed that a spherical indenter, rather sharp indenters with different shapes such as a Berkovich indenter, should be employed in composites nanoindentation experiments to avoid complicated phenomena. For example, a sharp indenter tip often leads to damage in matrices or interfaces. Moreover, numerical simulations show that plastic deformation occurs under very small indentation load due to the high stress concentration around the sharp tips [17].

2.2 Micromechanics characterization on the lower bound Young's moduli measured from elastic unloading curves

We assume that equation (3) is applicable to nanoindentation experiments of composite materials to simplify the data reduction, as suggested by Fischer-Cripps [28]. We also assume that three simplified zones on a composite surface as seen in Figure 3. These different material zones

can be determined by very different load-displacement data, plus direct observation on the material surface, for example, the naked fibers. But this examination is not necessary because our final conclusion is independent of these zones. Figure 3(a) illustrates a typical grid indentation on the surface of a composite specimen. If a sharp indenter tip indents on the fiber zone only, it will record a large reduced modulus compared with these indents on the pure matrix and the mixed fiber/matrix zones [19]. Meanwhile, the reduced moduli of the pure matrix and the mixed fiber/matrix zones are measured from other grid indentations, and these reduced moduli should be very different as illustrated in Figure 3(b).

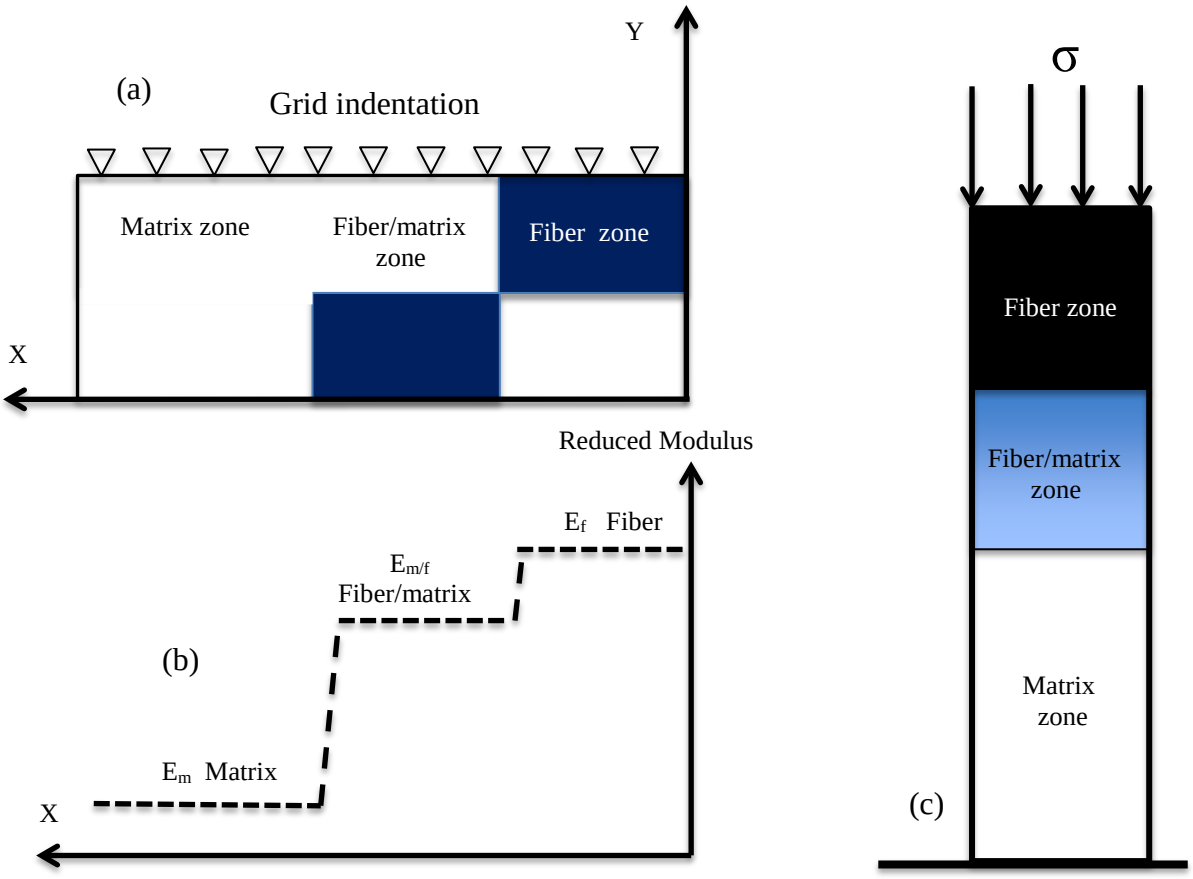

Figure 3. *Illustrations of (a) grid nanoindentation on a composite surface, (b) reduced modulus distributions, (c) a series model of the rule of mixture including the fiber and the matrix zones.*

If we measure many reduced moduli at different indentation locations, we cannot obtain the Young's modulus of a composite, which should be one value based on the volume average. Therefore, our focus turns to estimating the lower bound of the composite Young's modulus. In micromechanics of composite materials, there are two kinds of the rule-of-mixture models, i.e., the series rule-of-mixture model provides a lower bound of the composite Young's modulus, and the parallel rule-of-mixture model provides an upper bound of the modulus [21]. During the through-thickness indentation process, the fiber does not carry load at its two ends, therefore, the series rule-of-mixture model is the right model in this study.

As shown in Figure 3(c), the applied stress is the same for the fiber zone, the matrix zone and the mixed fiber/matrix zone in a series model. So the composite modulus E_{33} is determined by the average Young's moduli of the fiber, the matrix and the mixed fiber/matrix zones E_f, E_m, and $E_{f/m}$ and their volume percent V_f, V_m and $V_{f/m}$ (intermediate variables for the derivation purpose). Based on the linear elastic strain superposition principle, the total strain of the composite unit is:

$$\varepsilon_T = \frac{\sigma}{E_{33}} = \frac{\sigma V_f}{E_f} + \frac{\sigma V_m}{E_m} + \frac{\sigma V_{m/f}}{E_{m/f}} \tag{5}$$

Where V_f in equation (5) is not the common fiber volume percent of the composites, since there are some fibers in the mixed fiber/matrix zone too. From equation (2), the average Young's moduli in equation (5) could be replaced by their average reduced moduli measured on the specimen surface from the indentation tests, and we eliminate the common stress term σ:

$$\frac{1}{E_{33}} = \frac{V_f}{(1-\nu_f^2)E_r^f} - \frac{V_f(1-\nu_i^2)}{(1-\nu_f^2)E_i} + \frac{V_{m/f}}{(1-\nu_{m/f}^2)E_r^{m/f}} - \frac{V_{m/f}(1-\nu_i^2)}{(1-\nu_{m/f}^2)E_i} + \frac{V_m}{(1-\nu_m^2)E_r^m} - \frac{V_m(1-\nu_i^2)}{(1-\nu_m^2)E_i} \quad (6)$$

where E_r^f , E_r^m and $E_r^{f/m}$ are the average reduced moduli for the fiber, the matrix and the mixed fiber/matrix zones. Since the Young's modulus of the diamond indenter E_i is at least 1,000 GPa, which is much higher than the tensile moduli of the current fibers or matrices, all terms including $1/E_i$ are very small positive numbers which can be dropped. Therefore, $1/E_{33}$ has an upper limit:

$$\frac{1}{E_{33}} < \frac{V_f}{(1-\nu_f^2)E_r^f} + \frac{V_m}{(1-\nu_m^2)E_r^m} + \frac{V_{m/f}}{(1-\nu_{m/f}^2)E_r^{m/f}} < \frac{1}{(1-\nu_{max}^2)}\left[\frac{V_f}{E_r^f} + \frac{V_m}{E_r^m} + \frac{V_{m/f}}{E_r^{m/f}}\right] \quad (7)$$

The maximum Poisson's ratio ν_{max} (0.5) was used in equation (7) because the Poisson's ratio of the fiber/matrix zone is a variable which cannot not be measured. Finally, we obtain a lower bound of the through-thickness Young's modulus, which is based on the average reduced moduli:

$$E_{33} > (1-\nu_{max}^2)/\left[\frac{V_f}{E_r^f} + \frac{V_m}{E_r^m} + \frac{V_{m/f}}{E_r^{m/f}}\right] = 0.75/\left[\frac{V_f}{E_r^f} + \frac{V_m}{E_r^m} + \frac{V_{m/f}}{E_r^{m/f}}\right] \quad (8)$$

It is impossible to determine the volume percent of each zone, so we have to make some assumptions. If N_T is the total grid indentation number on the specimen surface, and N_f is the number of grid indentations on the fiber zone, then $V_f \approx N_f / N_T$, similarly, $V_m \approx N_m / N_T$ and $V_{f/m} \approx N_{f/m} / N_T$. Therefore, equation (8) could be further simplified as:

$$E_{33} > 0.75/\left[\frac{N_f}{N_T\, E_r^f} + \frac{N_m}{N_T E_r^m} + \frac{N_{m/f}}{N_T E_r^{m/f}}\right] \approx 0.75 N_T \left[\sum_{j=1}^{N_f} \frac{1}{E_r^{f,j}} + \sum_{j=1}^{N_m} \frac{1}{E_r^{m,j}} + \sum_{j=1}^{N_{f/m}} \frac{1}{E_r^{f/m,j}}\right]^{-1} \quad (9)$$

In the above derivation, since $1/E_r^j$ is an average parameter, $\frac{N_f}{E_r^f} \approx \sum_{j=1}^{N_f} \frac{1}{E_r^{f,j}}$, $\frac{N_m}{E_r^m} \approx \sum_{j=1}^{N_m} \frac{1}{E_r^{m,j}}$ $\frac{N_{m/f}}{E_r^{m/f}} \approx \sum_{j=1}^{\frac{N_f}{m}} \frac{1}{E_r^{\frac{f}{m},j}}$. Finally, a lower bound of the composite Young's modulus (only one value) could be obtained as the total contribution of each reduced indentation modulus as shown in equation (10):

$$E_{33} > 0.75 N_T \left[\sum_{j=1}^{N_T} \frac{1}{E_r^j}\right]^{-1} = \frac{0.75\ N_T}{\frac{1}{E_r^1} + \frac{1}{E_r^2} \cdots\cdots \frac{1}{E_r^{NT}}} \quad (10)$$

Before this inequation is used to deal with complicated composite or heterogenous materials, we should analyze the indentation of isotropic and homogenous materials. For example, if a diamond indenter is employed to ident an isotropic and homogenous specimen with a Young's modulus E (much lower than the Young's modulus of diamond) and a Poisson's ratios v . Based on equation (2), $\frac{1}{E_r^j} \approx \frac{1-v^2}{E}$. So equation (10) yields

$$E > \frac{0.75E}{1-v^2} \quad (11)$$

Because $1\text{-}v^2 > 0.75$, inequation (11) always holds for any isotropic and homogenous material with a Young's modulus E which is much smaller than 1,000 GPa. This simplified and compact

result will be very helpful to numerous nanoindentation users without any knowledge on micromechanics and indentation of composites.

3. Experimental Procedures

The composite material system tested was an E-glass fiber/Vinyl Ester (E-glass/VE) composite in the form of plain woven fabric composites (eight plies and the total laminate thickness 5 mm). This composite system was used to investigate the durability and dynamic failure properties in our previous studies [29]. The fiber volume percent was 54% after burn off testing. Nanoindentation tests were performed using a Hysitron TI 950 TriboIndenter™ nanoindentation system with a diamond Berkovich indenter [30]. All tests were conducted in load-controlled feedback mode to a peak force of 10 mN. First, a grid of 25 indents was performed on the matrix zone of the sample. A load function consisting of a five-second loading to peak force segment, followed by a five-second hold segment, and a one-second unloading segment was used. Next, lines of 10 indents were performed along the composite surface with the mixed fiber/matrix zone and the fiber zone. The hardness and reduced modulus of the matrix and fibers were then calculated from the initial unloading force versus the displacement curves. Indentation depths ranged from 300 nm to 1,300 nm.

Figure 4 compares the indentation force versus indentation depth curves from all series of indents performed on the composite sample [30]. The exposed fiber zone is considerably stiffer than the matrix and the fibers/matrix zones. The average diameter of this composite system is 10 μm. Figure 5(a) shows a scanning probe microscope image of the surface of the matrix zone after one representative indent was performed. Figure 5(b) shows a scanning probe microscope image of an exposed fiber after one representative indent was performed. The difference in mechanical properties of the matrix and the exposed fibers can be clearly seen when comparing the sizes of

two residual indents under the same indentation force. Usually, fibers have much higher Young's moduli/hardness and yielding strengths than polymeric matrices [21], therefore, their residual indent shapes are smaller.

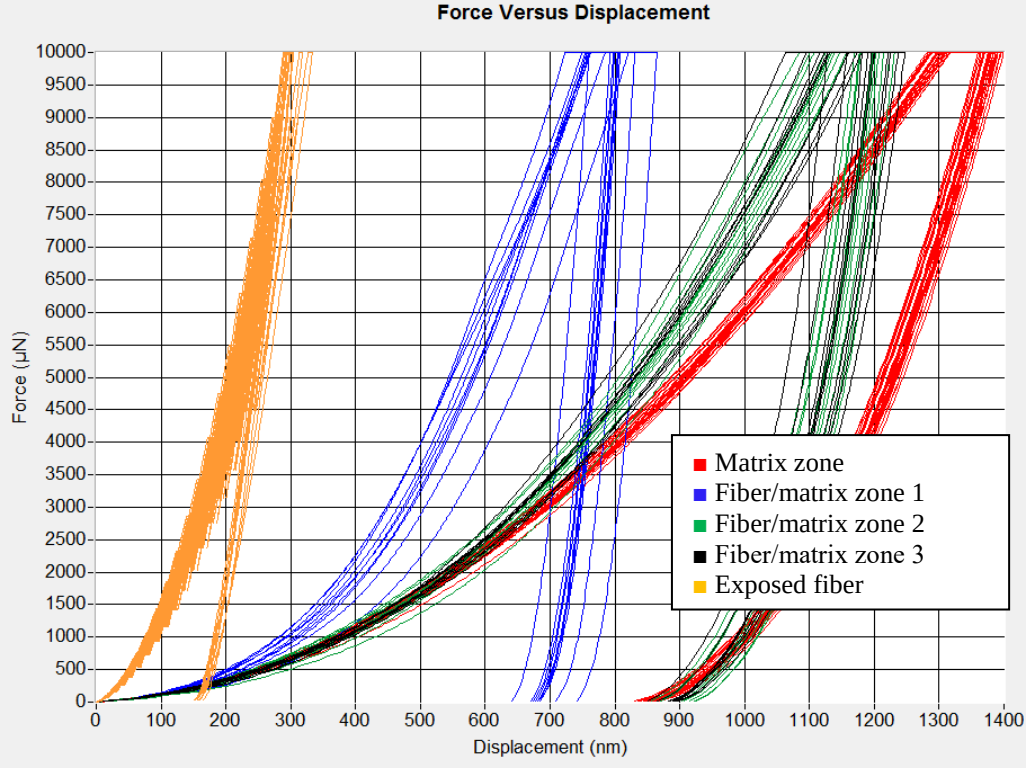

Figure 4. *Indentation force versus indentation displacement from each set of indents performed on the composite sample.*

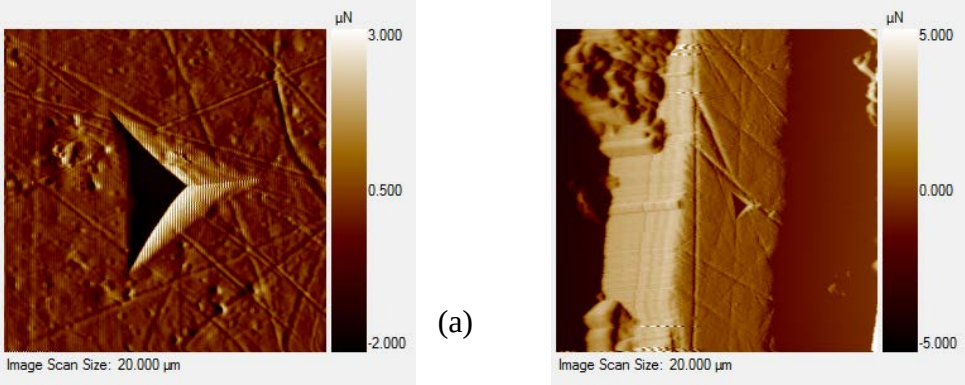

Figure 5 (a) *Scanning probe microscope images of the surfaces of the matrix zone (thin lines are not fibers), and (b) exposed fiber with a small indent on the same composite sample. Permanent deformation on the fiber is much smaller than the deformation of the matrix due to its high stiffness and yielding strength.*

Table 1. Average hardness, reduced moduli measured from the different locations of the composite sample surface

Sample	Number of tests	Hardness (GPa)	Reduced modulus (GPa)
Pure matrix zone	n=25	0.27 ± 0.005	5.52 ± 0.53
Fiber/matrix zone 1	n=10	0.62 ± 0.044	33.47 ± 1.15
Fiber/matrix zone 2	n=10	0.35 ± 0.013	12.13 ± 0.18
Fiber/matrix zone 3	n=10	0.36 ± 0.017	12.30 ± 1.37
Exposed fibers	n=13	~6.0 to 7.5	~65.0 to 85.0

4. Results and Discussion

Table 1 compares the hardness and reduced moduli of each zone. For the matrix and the fiber/matrix zones, average values are shown. While for the exposed fiber zone, a range of the hardness (from 6.0 to 7.5 GPa) and the reduced moduli (from 65.0 to 85.0 GPa) are provided. Using equation (10) and data from Table 1, we find that the lower bound of the composite Young's modulus is 7.68 GPa. While the average through-thickness composite Young's modulus measured from a spherical indentation was 12.36 ± 4.13 GPa or 8.23 ~ 16.49 GPa [22]. Therefore, 7.68 GPa is indeed a measured lower bound since it is smaller than the directly measured Young's modulus. Moreover, the lower bound modulus could be predicted by the series rule-of-mixture model using the composite fiber volume percent 54% [21]. The tensile moduli of the matrix and the fiber of the E-glass/VE composite system are 3.40 GPa and 70.00 GPa respectively [31-32], so the theoretical lower bound of the composite modulus (predicted using the series rule-of-mixture model) is 6.85 GPa, which is quite close to the experimental lower bound 7.68 GPa. We notice that the measured

lower bound is much larger than the matrix modulus. This result demonstrates that our measurement includes the modulus contributions from these stiff fibers, and the soft matrix.

The separation of two indentations is a key parameter for measurements. Because one damage/plastic zone occurs after a high-load indentation, the next indentation should have an enough distance from this damage zone to ensure the same measurement conditions. This damage zone is related to not only the maximum indentation depth, but also the indenter sizes, and the properties of fibers and matrices. In this project, the average diameter of the glass fiber was around 10 μm, the edge length of a square composite representative volume element (RVE based on 54% fiber volume percent) was around 12.5 μm. Because the indentation depths ranged from 300 nm to 1,300 nm (1.3 μm), we believe that the RVE is fully deformed and permanent deformation existed (at least 10 μm as shown in Figure 5(a)). Permanent deformation should exist in its surrounding RVEs. So, we suggest that the minimum separation of two indentations would be around 5-10 times of the size of an RVE. For our experiment, the minimum separation of two indentations was around 100 μm. Based on our previous composite indentation and finite element analysis [3,22], the suggested separation of two indentations is around 200 μm for most composites or heterogenous materials with very different sizes of reinforcements. The grid indentation number along one direction (x or y) is simply determined by the specimen length/200 μm. Indeed, the measurements of our approach are related to many factors such as the indenter type and the maximum indentation depth. However, a sophisticated and universal approach is not available, so our simplified approach at least can yield reasonable measurement.

The measurements and the theoretical prediction of the lower bound Young's moduli of composite materials provide an efficient solution of a complicated mechanics/material problem. For example, Deng et al. measured the Young's modulus of a multilayered composite with

complex substrate effect using nanoindentation (E_{33}=71 GPa), which was between their micromechanics predictions of the upper bound value (103 GPa) and the lower bound value (55 GPa) using two rules of mixture [33]. In this paper, we mainly measured, not predicted the lower bound value. Randall et al. also reported a similar lower bound estimation of the indentation Young's moduli for particle-reinforced composites [34]. Indeed, our approach can be extended to particle-reinforced composites or other heterogeneous materials. Our major improvement compared to previous research is that we have a correction factor due to the Poisson's ratios. Therefore, our lower bound modulus is always smaller than the previous estimation by Randall et al [34]. For any structure material, a measured low material property is much more important than a measured high property due to safety concern. For example, we measure a series of material fracture toughness values from different specimens with different thicknesses for the same material. However, we only employ the smallest fracture toughness value measured from the thick specimen under the plane-strain condition for damage tolerance designs. Therefore, our lower bound estimation will enhance the safety of composite material designs.

4. Conclusion

A lower bound approach to measure the through-thickness Young's modulus of a composite material based on local indentation reduced moduli is proposed. This simplified approach was applied to grid nanoindentation of a glass-fiber composite material system, and the result showed that the experimental lower bound was around 40% lower than the measured Young's modulus of the same composite system using nanoindentation and Hertz's contact law. The experimental lower bound is close to the theoretical bound based on micromechanics analysis. Therefore, the proposed approach provides a conservative measurement if the actual through-

thickness Young's modulus is not available. The proposed approach is helpful for these nanoindentation users without comprehensive knowledge of micromechanics and contact mechanics to deal with complicated indentation for composites or heterogenous materials.

Acknowledgements

The authors acknowledge the support from the Air Force Office of Scientific Research (grant number FA9550-18-1-0006, Dr. Jaimie Tiley, Program Officer). Valuable discussion and measurement results from Dr. A. Fischer-Cripps and Ms. A. Simpson are appreciated. We also thank the reviewers for their suggestions and comments to improve the original manuscript.

Reference

1. Krishnan A, Xu LR (2011) A short-beam shear fracture approach to measure the mode II fracture toughness of materials with preferred interfaces. Int J Fract 169:15–25.
2. Wei X, Kysar JW (2012) Experimental validation of multiscale modeling of indentation of suspended circular graphene membranes. Int J Solids Struct 49:3201-3209.
3. Martinez R, Xu LR (2014) Comparison of the Young's Moduli of Polymers Measured from Nanoindentation and Bending Experiments. MRS Communications 4:89-93
4. Singh DRP, Chawla N, Shen YL (2010) Nanoindentation Measurement of Surface Residual Stresses in Particle-Reinforced Metal Matrix Composites. Mater Charact 61:481-488
5. Cao G, Chen X, Xu ZH, Li X (2010) Measuring mechanical properties of micro- and nano-fibers embedded in an elastic substrate: Theoretical framework and experiment. Compos Part B-Eng 41:33-41
6. Lu YC, Jones DC, Tandon GP, Putthanarat S, Schoeppner GA (2010) High Temperature Nanoindentation of PMR-15 Polyimide. Exp Mec 50:491-49
7. Willis JR (1966) Hertzian contact of anisotropic bodies, J Mech Phys Solids 14:163-176
8. Heinrich C, Waas AM, Wineman AS (2009) Determination of material properties using nanoindentation and multiple indenter tips. Int J Solids Struct 46:364-376
9. Vlassak JJ, Ciavarella M, Barber JR, Wang X (2003). The indentation modulus of elastically anisotropic materials for indenters of arbitrary shape. J Mech Phys Solids 51: 1701-1721
10. Jorgensen O, Giannakopoulos AE, Suresh S (1998) Spherical indentation of composite laminates with controlled gradients in elastic anisotropy. Int J Solids Struct 35:5097-5113
11. Johnson KL (1985) Contact Mechanics. Cambridge, England
12. Delafrague A, Ulm FJ (2004) Explicit approximations of the indentation modulus of elastically orthotropic solids for conical indenters. Int J Solids Struct 41:7351-7360.
13. Gregory JR, Spearing SM (2005) Nanoindentation of neat and in-situ polymers in polymer-matrix composites. Compos Sci Technol 65:595-607.
14. Gao YF, Pharr GM (2007) Multidimensional contact moduli of elastically anisotropic solids. Scripta Mater 57:13-16.
15. Ghosh D, Subhash G, Sudarshan TS, Radhakrishnan R, Gao XL (2007) Dynamic Indentation Response of Fine-Grained Boron Carbide. J Am Ceram Soc 90:1850-1857
16. Nakamura T, Gu Y (2007) Identification of elastic–plastic anisotropic parameters using instrumented indentation and inverse analysis. Mech Mater 39:340-356
17. Rittel BP, Ravichandran G (2008) An analysis of nanoindentation in linearly elastic solids. Int J Solids Struct 45:6018–6033
18. Yedla SB, Kalukanimuttam M, Winter RM, Khanna SK (2008) Effect of Shape of the Tip in Determining Interphase Properties in Fiber Reinforced Plastic Composites Using Nanoindentation. J Eng Mater-T 130:41010-041025
19. Hardimana M, Vaughanb TJ, McCarthy CT (2015) Fibrous composite matrix characterization using nanoindentation: The effect of fibre constraint and the evolution from bulk to in-situ matrix properties. Compos Part A-Appl S 68:296-303
20. Wu YF, Yu HY, Chen WQ (2012) Mechanics of indentation for piezoelectric thin films on elastic substrate, Int J Solids Struct 49:95-110
21. Daniel I, Ishai O (2006) Engineering mechanics of composite materials. London, England

22. Martinez R, Xu LR (2018) Measurements of the Approximate Through-Thickness Young's Moduli of Fibrous Composite Laminates using Nanoindentation. Submitted for publication.
23. Fischer-Cripps AC (2011) Nanoindentation. New South Wales, Australia
24. Oliver WC, Pharr GM (1992) An improved technique for determining hardness and elastic modulus using load and displacement sensing indentation experiments. J Mater Res 7:1564-1583
25. Cheng YT, Cheng CM (2005) Relationships between initial unloading slope, contact depth, and mechanical properties for conical indentation in linear viscoelastic solids. J Mater Res 20:1046-1053
26. Huang G, Hongbing L (2006) Measurement of Young's relaxation modulus using nanoindentation. Mech Time-dependent Mater 10.3:229-243
27. Xu LR, Rosakis AJ (2002) Impact failure characteristics in sandwich structures: Part I: Basic failure mode selection. Int J Solids Struct 39:4215-4235
28. Xu LR and Rosakis AJ (2005) Impact damage visualization of heterogeneous two-layer materials subjected to low-speed impact. Int J Damage Mech 14:215-233
29. Fischer-Cripps A (2010) Fischer-Cripps Laboratories Pty Ltd. Private communication
30. Simpson A (2011) Hysitron Inc. Minneapolis, MN. Private communication.
31. Xu LR, Krishnan A, Ning H; Vaidya U (2012) A seawater tank approach to evaluate the dynamic failure and durability of E-glass/vinyl ester marine composites. Compos Part B-Eng 43:2480-2486
32. Yan H, Oskay C, Krishnan A, Xu LR (2010) Compression After Impact Response of Woven Fiber-Reinforced Composites. Compos Sci Technol 70:2128-2136
33. Deng X, Nikhilesh C, K Chawla, M Koopman, J Chu (2005) Mechanical Behavior of Multilayered Nanoscale Metal-Ceramic Composites. Adv Eng Mater 7:1099-1108
34. Randall NX, Vandamme M, Ulm FJ (2009) Nanoindentation analysis as a two-dimensional tool for mapping the mechanical properties of complex surfaces. J Mater Res 24:679-90